Journal of Geophysical Research: Space Physics

RESEARCH ARTICLE
10.1002/2017JA024904

Dipolarization Fronts With Associated Energized Electrons in Saturn's Magnetotail

A. W. Smith[1], **C. M. Jackman**[1], **M. F. Thomsen**[2], **N. Sergis**[3,4], **D. G. Mitchell**[5], **and E. Roussos**[6]

[1]Department of Physics and Astronomy, University of Southampton, Southampton, UK, [2]Planetary Science Institute, Tucson, AZ, USA, [3]Office of Space Research and Technology, Academy of Athens, Athens, Greece, [4]Institute of Astronomy, Astrophysics, Space Applications and Remote Sensing, National Observatory of Athens, Athens, Greece, [5]Applied Physics Laboratory, The Johns Hopkins University, Laurel, MD, USA, [6]Max-Planck-Institut für Sonnensystemforschung, Goettingen, Germany

Key Points:
- Automated methods used to identify coincident southward field rotations and electron energizations
- Dipolarizing material shows a systematic increase in electron temperature and reduction in density
- Electron heating and density changes exhibit a larger range of variation postmidnight

Correspondence to:
A. W. Smith,
aw.smith@soton.ac.uk

Citation:
Smith, A. W., Jackman, C. M., Thomsen, M. F., Sergis, N., Mitchell, D. G., & Roussos, E. (2018). Dipolarization fronts with associated energized electrons in Saturn's magnetotail. *Journal of Geophysical Research: Space Physics*, *123*, 2714–2735. https://doi.org/10.1002/2017JA024904

Received 19 OCT 2017
Accepted 19 MAR 2018
Accepted article online 26 MAR 2018
Published online 19 APR 2018

Abstract We present a statistical study of dipolarization fronts within Saturn's magnetotail. Automated methods were used to identify 28 significant southward rotations of the field coupled with enhancements in the electron energy. The observed dipolarizations cover the majority of the magnetotail, though possess a strong dawn-dusk asymmetry (79% occur postmidnight). Almost half (43%) of dipolarizations occur within 3 hr of another event, though these chains are solely observed postmidnight. Most pitch angle distributions of the heated electron populations show increased relative fluxes parallel or perpendicular to the field, likely due to nonlocal heating effects. The electron temperature and density following the passage of a front are anticorrelated; the temperature increases are accompanied by a decrease in their density. The temperature increases by factors of 4–12, while the density drops by factors of 3–10. Premidnight events consistently show the smallest relative heating and density depletion, suggesting they are observed closer to their generation. In contrast, the location of the postmidnight x-line is inferred to be more variable, with a large variety of heating factors observed. Forty percent of the events show a strong reduction in water (W^+) group fraction, likely related to either the preferential loss of equatorial heavy ions in departing plasmoids or the closure of open field. Two of these events show significant compositional changes suggesting the addition of plasma of external origin; we suggest that these events involved the closure of open field.

1. Introduction

Dipolarization fronts are localized increases in the north-south component of a planetary magnetic field that propagate toward the planet. Dipolarization fronts have been observed for many years at the Earth (e.g., Nakamura et al., 2002; Ohtani et al., 2004; Runov et al., 2009). The accompanying inward moving plasma populations are known as bursty bulk flows (Angelopoulos et al., 1992, 1994; Baumjohann et al., 1990; Cao et al., 2006). More recently, analogous signatures have been observed at Mercury (e.g., Sun et al., 2016; Sundberg et al., 2012), Jupiter (e.g., Kasahara et al., 2011; Vogt et al., 2010), and Saturn (e.g., Bunce et al., 2005; Jackman et al., 2015). They are thought to form as a result of reconnection within a planetary magnetotail (Ashour-Abdalla et al., 2015; Fu et al., 2013; Runov et al., 2012; Sitnov et al., 2009). The newly reconnected magnetic field lines are expelled from the planetward side of the reconnection site, retracting toward the planet under the influence of magnetic tension forces. At Earth, the cross-tail width of these structures has been estimated to be ~10% of the width of the terrestrial magnetotail or smaller (Angelopoulos et al., 1996; Nakamura et al., 2004). At Jupiter, Vogt et al. (2010) similarly estimated the width of the associated flow channels to be ~5–10% of the magnetotail.

Previous work at the Earth has found that dipolarization fronts are often associated with increases in the flux of high-energy electrons (Asano et al., 2010; Duan et al., 2014; Runov et al., 2009, 2013). For the majority of terrestrial events the increase in high-energy electrons (>1 keV) is accompanied by a decrease in the fluxes at lower energies (<1 keV; Deng et al., 2010; Pan et al., 2014; Runov et al., 2013). The dipolarization front itself is thought to be of the order of the ion thermal gyroradius (or inertial length) thick (Deng et al., 2010; Duan et al., 2014; Hwang et al., 2011; Runov et al., 2009, 2011). The front separates the cooler, denser ambient plasma

sheet planetward of it from a hotter, more tenuous region that follows its passage (Runov et al., 2015). The dispersionless nature of the increase in energetic electron flux (Apatenkov et al., 2007) suggests that the generation of the hotter plasma is either linked to the origin of the dipolarization front or its propagation (Duan et al., 2014). The high-energy electron population is sometimes observed to be anisotropic with respect to pitch angle (PA, α), with some examples showing peaks around $\alpha = 90°$ (Asano et al., 2010), while others show peaks closer to $\alpha = 0°$ and 180° (Birn et al., 2014; Runov et al., 2013). The PA distribution observed is often a function of the energy (Apatenkov et al., 2007; Runov et al., 2012).

There are two broad categories of mechanisms that have been suggested to heat the plasma behind the dipolarization front: processes at the reconnection site itself ("local heating") (e.g., Fu et al., 2017; Øieroset et al., 2002), and those that occur during the planetward transport of the plasma ("nonlocal heating"). Local heating is thought to be dominated by anisotropic heating via parallel electric fields (Asano et al., 2010; Egedal et al., 2008). Nonlocal mechanisms include adiabatic betatron and Fermi accelerations (e.g., Ashour-Abdalla et al., 2011; Birn et al., 2014; Gabrielse et al., 2017; Pan et al., 2014) and nonadiabatic wave-particle interactions (e.g., Deng et al., 2010; Huang et al., 2012, 2015; Grigorenko et al., 2017). Some combination of both local and nonlocal heating is possible; indeed, some observations have suggested that different mechanisms dominate for different ranges of energy (Ashour-Abdalla et al., 2011; Duan et al., 2014; Pan et al., 2014). In general, betatron acceleration would be expected to increase the energies perpendicular to the magnetic field, while Fermi heating affects those parallel/antiparallel to the field. Analysis of the PA distributions can therefore elucidate the dominant mechanism at a given energy range (e.g., Birn et al., 2014; Runov et al., 2012). Care must be taken, however, as new plasma is introduced during the propagation of the front, and so the plasma is not necessarily representative of the population at the reconnection site (Eastwood et al., 2015). Additionally, such signatures can be damped due to scattering.

At Saturn a dipolarization front was first observed during the outbound pass of Cassini's SOI (Saturn Orbit Insertion) (Bunce et al., 2005). In this event the Cassini spacecraft observed the sudden arrival of a hot tenuous plasma population accompanying a sharp rotation of the magnetic field. As Saturn's magnetic field has the opposite orientation to the Earth, the deflections associated with Kronian dipolarization fronts are southward (as opposed to typical terrestrial northward turn). More recent Kronian studies have located dipolarization fronts either from their southward rotation of the magnetic field (Jackman et al., 2013, 2015; Russell et al., 2008; Smith et al., 2016; Yao, Grodent, et al., 2017) or from the presence of an inflowing (Thomsen et al., 2013) or heated plasma population (Thomsen, Mitchell et al., 2015). In contrast to the Earth, the Saturn equivalent of bursty bulk flows may not be expected to show a dominant planetward component; any radial inflow must combine with the strong azimuthal corotational flow (Mcandrews et al., 2009; Thomsen et al., 2013).

The Kronian dipolarizations present in the literature vary somewhat in the individual signatures displayed. A southward rotation of the magnetic field is the most common diagnostic of these events and is present in all but one of the published examples (Thomsen et al., 2013, Figure 10). The presence of a heated electron population following the front is not observed in all examples (e.g., Jackman et al., 2013; Russell et al., 2008). Overall however, the presence of energetic electrons have only ever been observed in those events that display a strong rotation of the magnetic field; although this could be a selection effect as the majority of events have been selected on the basis of their magnetic field signature.

At Earth reconnection on the dayside magnetopause leads to the opening of planetary magnetic flux and introduces mass to the system. The newly "opened" flux is transferred across the polar caps and into the magnetotail lobes where it can drive tail reconnection, closing the flux and releasing mass down the magnetotail. This cyclical process is known as the Dungey cycle (Dungey, 1961). At Saturn and Jupiter the presence of significant internal mass sources (Enceladus and Io, respectively) coupled with their fast planetary rotation rates leads to an internally driven cycle: the Vasyliunas cycle (Vasyliunas, 1983). In this cycle, as mass-loaded flux tubes rotate around the dusk flank, they are no longer supported by the magnetopause and begin to stretch down the magnetotail. Eventually, these flux tubes pinch off, releasing the internally generated mass down the magnetotail. In contrast to the Dungey cycle, this process does not open or close magnetospheric flux. Both cycles can in principle operate at Saturn, but the degree to which the Dungey cycle operates or impacts large-scale dynamics is debated (e.g., Badman & Cowley, 2007; Delamere et al., 2015).

Saturn's magnetosheath contains high beta plasma and strong low-latitude shear flows, inhibiting reconnection for all but high magnetic shear regions (Desroche et al., 2013; Masters, 2015; Masters et al., 2012).

Despite these constraints, in situ evidence for magnetopause reconnection has been observed (Fuselier et al., 2014; Jasinski et al., 2014, 2016; Lai et al., 2012; McAndrews et al., 2008). The presence of dayside reconnection necessitates the subsequent closure of flux within the magnetotail, namely, the Dungey-type reconnection. A potential discriminator between the products of internally generated Vasyliunas-type and externally driven Dungey-type reconnection is the composition of the plasma within the dipolarizing region. The majority of Kronian dipolarizations reported to date show strong signatures of water group ions (henceforth, referred to as W+, originating from Enceladus), suggesting they are Vasyliunas cycle related (e.g., Jackman et al., 2015; Masters et al., 2011; Mitchell et al., 2005; Thomsen et al., 2013; Thomsen, Jackman, et al., 2015). However, Thomsen, Jackman, et al., (2015) reported a long duration W+ depleted inflow, suggested to be the result of Dungey-type reconnection following a solar wind-driven magnetospheric compression.

The aim of this work is to investigate the morphology, distribution, and plasma character of Kronian dipolarizations. Section 2 of the paper will concern the instruments and data used in this study. Section 3 will summarize the techniques used to identify the relevant signatures. Section 4 will then discuss the identified events and their morphology. This will be followed in section 5 with a discussion of their spatial and temporal distribution. Section 6 will then investigate the energization of the observed plasma population. Finally, the relative composition of the heated material will be discussed in section 7.

2. Data

Magnetic field data for this study come from the Cassini magnetometer (Dougherty et al., 2004). The Kronocentric radial theta phi (KRTP) coordinate system is used; this is a spherical polar system: B_r (the radial component) is positive radially outward from Saturn, B_θ (the meridional component) is positive southward, and B_ϕ (the azimuthal component) is positive in the direction of corotation. Jackman et al. (2009) showed that this system is suited to distinguish the magnetic signatures due to magnetotail dynamics from other phenomena (e.g., periodic encounters with the magnetotail plasma sheet). Events were identified using data with a 1 min cadence; the average duration of a magnetically identified planetward moving event has been found to be ~5 min (Smith et al., 2016).

Data from Cassini Plasma Spectrometer (CAPS) are used to investigate the in situ plasma properties (Young et al., 2004). The Cassini Electron Spectrometer (ELS) is an electrostatic analyzer, recording electrons between 0.58 and 26,000 eV. In general, the ELS instrument does not sample the full 4π sr of the sky, unless Cassini happens to be rolling during the interval of interest. The instrument is mounted on an actuating platform and thus samples $\sim 2\pi$ sr of the sky. However, in general, the bulk velocity of the electrons in Saturn's magnetosphere is much less than their thermal velocity, meaning the actuation of the instrument generally gives fairly complete PA distributions within the CAPS energy range (Arridge, McAndrews, et al., 2009). For this reason any signature of a dynamic event/change in the electron population should be observable regardless of the direction in which CAPS is pointing. The data presented for this study are mostly A cycle and anode averaged fluxes: flux averaged over 16 consecutive energy sweeps and all 8 anodes. The data are also corrected using geometric factors and energy-dependent efficiencies. For more information on the generation of this data the interested reader is directed to Thomsen et al. (2016). Electron moments such as temperature and density are also used (Waite & Furman, 2013); the techniques that are used to generate the moments are described by Lewis et al. (2008) and Arridge, Gilbert, et al. (2009). The CAPS ion mass spectrometer is also used to ascertain flow directions.

Data from the Magnetospheric Imaging Instrument (MIMI) (Krimigis et al., 2004) are used to complement the CAPS observations at higher energies. The Low-Energy Magnetospheric Measurement System (LEMMS) is one of the three instruments that comprise MIMI. LEMMS measures electrons between 20 keV and several MeV. LEMMS is mounted upon a rotating platform designed to allow sampling of a greater fraction of the three-dimensional energetic particle distribution; however, during the epochs explored by this work the platform did not rotate and thus LEMMS samples a smaller region of sky (and PAs relative to the field). Data from the Charge Mass Spectrometer (CHEMS) instrument are also used by this study. CHEMS is able to measure both the mass and mass per charge of ions with energies between 3 and 236 keV for H^+ and between 8 and 236 keV for O^+. CHEMS is particularly useful in distinguishing ion species with identical m/q ratios and different atomic masses (e.g., H_2^+ and He^{++}). The final constituent of MIMI is the Ion and Neutral Camera (INCA). INCA can record the energy, direction and rough composition of ions between ~7 keV and 3 MeV.

INCA has a field of view of 120° by 90°. When combined with simultaneous magnetometer data, INCA can provide detailed PA analysis of the energetic particles within its field of view.

Data from Cassini's orbits in 2006, late 2009, and 2010 were investigated; this combination of data provide good magnetotail coverage at midnight and dawn (2006), as well as at dusk (late 2009 and 2010). A list of magnetopause crossings was used to exclude data from the magnetosheath and solar wind (Pilkington et al., 2015). Additionally, data from the dayside ($X_{KSM} \geq 0$) and that obtained within a radial distance of 15 R_S were also excluded from the analysis to allow the focus on magnetotail dynamics. Within ~15 R_S the magnetic field becomes more quasi-dipolar, and selecting significant southward field deflections becomes more difficult against the larger background field (Arridge et al., 2011).

3. Event Signature and Selection Method

Figure 1 shows an example of a Kronian dipolarization. Figures 1a–1d show the magnetic field in KRTP coordinates, while Figure 1e shows an ELS flux spectrogram. The signatures in both the magnetic field and the energy-flux spectrogram are used to identify the event. The methods by which the relevant magnetic and plasma signatures are located in the data are briefly discussed below. For more details the interested reader is directed to Appendices A and B.

3.1. Magnetic Field Deflection

A key signature of a dipolarization is the sharp rotation of the magnetic field in the north-south meridian (an increase in the B_θ component): highlighted in Figure 1b between the vertical dashed lines. Smith et al. (2016) recently developed a technique to locate magnetic field deflections greater than background fluctuations of the field. Smith et al. (2016) set the threshold such that deflections must be greater than 1.5 B_θ^{RMS} (root-mean-square) of the field, calculated for an hour interval surrounding the deflection. In this work, the effect of lowering this threshold is considered for targeted intervals. The method is described in more detail in Appendix A. In the case of the event in Figure 1, strong planetward flows precede the magnetic signature (discussed in section 4.3, Figure 2), suggesting that the magnetic dipolarization is embedded in the high speed flow.

3.2. Electron Energy Enhancement

Terrestrial dipolarization fronts in the literature often involve a magnetic deflection accompanied by a plasma signature: this generally comprises an increase in the flux of higher-energy electrons combined with a simultaneous reduction in the fluxes at lower energies (Deng et al., 2010; Pan et al., 2014; Runov et al., 2013). This combination leads to an arc-like signature in an electron spectrogram, for example, that shown in Figure 1e centered at around 13:50. Before this time, between 13:15 and 13:40, the main electron population extends between ~20 eV and 1 keV, suggesting Cassini is within the magnetotail plasma sheet (Arridge, McAndrews, et al., 2009). Following the magnetic field deflection at 13:35, and for approximately 15 min, the spacecraft is engulfed by a higher-energy population of electrons (~300 eV–5 keV). The population returns to something more akin to the previous plasma sheet distribution at approximately 13:55. To locate this arc-like signature a statistical method has been developed. The method is based around quantile-quantile (QQ) plots (Gilchrist, 2000), a technique that allows the direct comparison of two distributions without requiring them to be fit to a model. More details on the application of the technique are given in Appendix B.

4. Identifications and Morphology

In total 712 significant ($\Delta B_\theta \geq 1.5 B_\theta^{RMS}$) southward magnetic field deflections (termed MAG detections) were located within the data set (Smith et al., 2016). In contrast, only 58 intervals of electron energization (termed ELS detections) were identified independently within the same interval of data. When the two sets of detections were cross referenced a total of 17 events were found that exhibited both signatures. Upon manual inspection of the 58 ELS detections, it was found that more than 17 were coincident with southward rotations of the field, although the magnitude of some of the deflections was below the empirical threshold ($\Delta B_\theta \leq 1.5 B_\theta^{RMS}$). Lowering the threshold for magnetic field deflections to $\Delta B_\theta \geq B_\theta^{RMS}$ increased the number of coincident electron and magnetic field signatures to 28. These 28 dipolarizations form the catalog of events for further investigation in this study. A summary of the events and their properties is provided in Table 1.

Table 2 displays a list of dipolarizations from the literature for comparison with our results. For example, only the dipolarizations reported by Bunce et al. (2005), Thomsen, Jackman, et al. (2015), and one of those identified

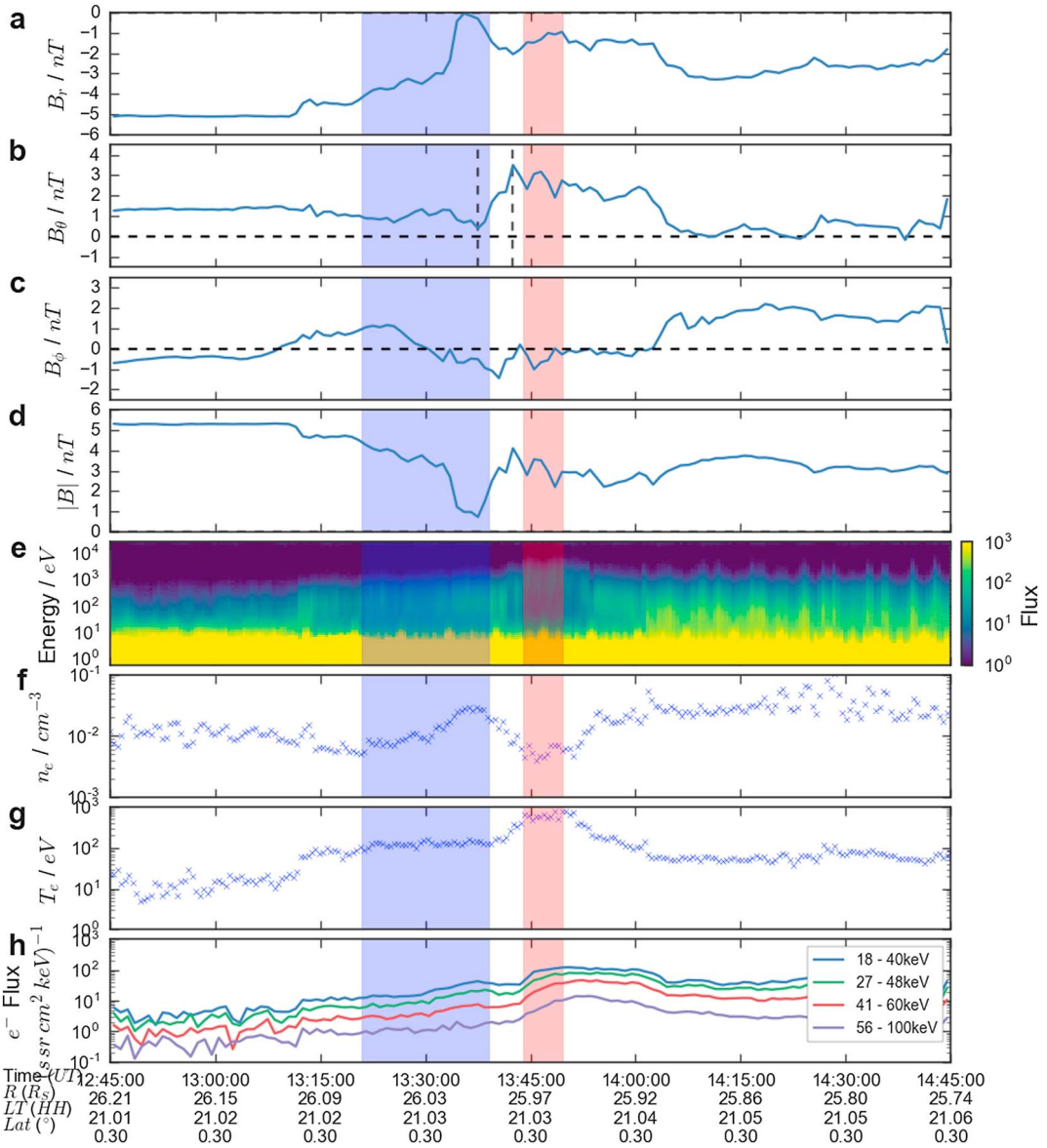

Figure 1. One hour of Cassini data from day 341 2009. (a–d) Magnetometer data in the Kronocentric radial theta phi coordinate system. (e) An electron spectrometer flux spectrogram. (f) Electron density and (g) temperature moments (the methods by which they are calculated are described by Lewis et al., 2008 and Arridge, Gilbert, et al., 2009). (h) The differential electron flux from the Low-Energy Magnetospheric Measurement System instrument in channels ranging between 18 and 100 keV. The blue shaded region was identified by the technique described in section 3.2 as the background plasma sheet, while the red shaded region was identified as the energetic electron population following the dipolarization front. The black vertical dashed lines in Figure 1b bracket the magnetic field deflection of interest.

by Thomsen (2013) show both the magnetic field and electron signatures typical of a terrestrial dipolarization front. It should also be noted that our methods were capable of locating the magnetic and electron signatures of all the events in Table 2.

4.1. Dipolarizations Lacking an Energetic Electron Signature

As outlined above, the vast majority ($^{695}/_{712}$) of significant southward magnetic field deflections are unaccompanied by the expected electron signature of a dipolarizations front. Looking to the literature, the two dipolarizations discussed by Russell et al. (2008) and Jackman et al. (2015) both lacked electron heating signatures and were observed while Cassini was at a relatively large distance from the current sheet center ($|B_R| \geq 2$ nT). Far from the center of the current sheet the electron counts can be expected to be relatively weak. It is therefore possible that these events did result in electron heating, but that this heated

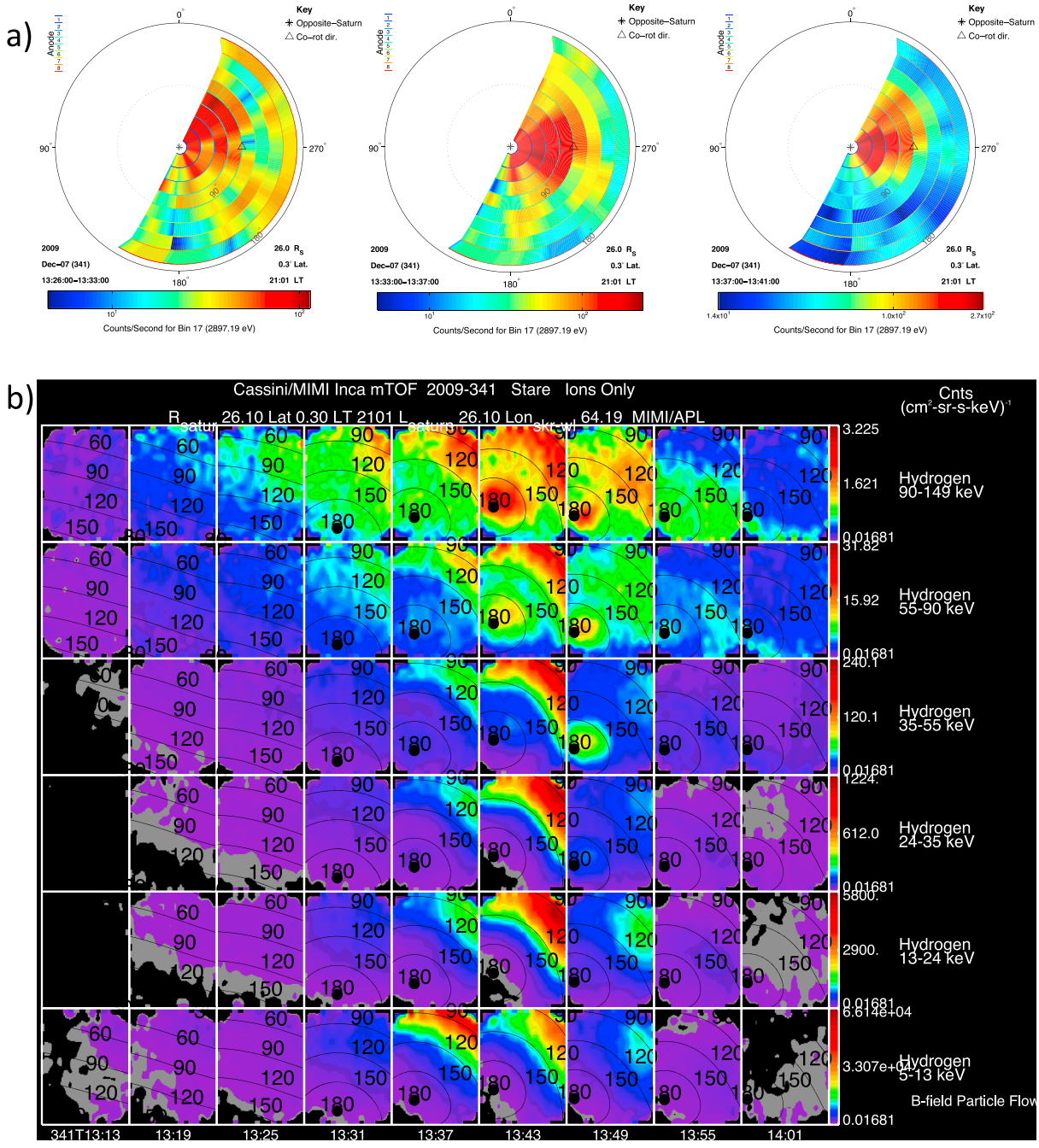

Figure 2. (a) Cassini Plasma Spectrometer/ion mass spectrometer all-sky images for three intervals around the dipolarization in Figure 1. The center of each plot represents the antisaturnward look direction (as if the observer is looking along the radial unit vector of the planet), and the radial distance away from the center is proportional to the polar angle relative to the antisaturnward direction. Therefore, the dashed circle represents a direction 90° from the radial direction, and the outside of the circle represents the saturnward direction. The corotational direction is indicated by the triangle on the right-hand side of each circle. The colors indicate the counts per second at an energy per charge of 2,897 eV. The times used to integrate the counts are shown below each panel. White regions correspond to look directions not covered by Cassini Plasma Spectrometer in this interval. (b) INCA angular distributions for H+ between 13:13 and 14:01. Pitch angle contours are shown in black for 60°, 90°, 120°, and 150°. The panels advance in time across the bottom axis and increase in energy moving up the panels. Note that the color bars showing counts $(cm^2 \cdot sr \cdot s \cdot keV)^{-1}$ are different for each row (energy). INCA = Ion and Neutral Camera; MIMI = Magnetospheric Imaging Instrument.

Table 1
Catalog of Kronian Dipolarizations and Properties

	Date and Time	$\lvert\Delta B_\theta\rvert$ / nT	LT / HH	R / R_S	Lat / deg	Group/ isolated	CAPS/ ELS moments?	PA spectra (FA/P/none)[a]	LEMMS e^-?	CHEMS?
0	4/3/2006 00:41	−0.98	3.00	42.01	0.14	I	N	–	N	N
1	18/3/2006 04:24	−3.98	5.88	25.93	−0.15	I	N	–	N	N
2	25/4/2006 02:40	−1.77	5.12	33.72	−0.07	G	N	–	Y	N
3	25/4/2006 02:40	−1.77	5.12	33.72	−0.07	G	N	–	Y	N
4	25/4/2006 13:54	−1.44	5.31	31.07	−0.09	I	Y	FA	Y	Y
5	19/5/2006 19:49	−1.83	4.02	25.35	0.02	I	Y	FA	Y	N
6	20/5/2006 06:37	−2.87	4.30	22.36	0.00	G	Y	FA	N	N
7	20/5/2006 07:09	−2.26	4.32	22.18	−0.01	G	N	–	N	N
8	20/5/2006 07:35	−2.08	4.33	22.10	−0.01	G	Y	FA	N	N
9	21/5/2006 04:01	−3.68	5.35	15.25	−0.12	I	Y	FA	Y	Y
10	21/7/2006 21:16	−4.71	2.42	21.76	0.33	I	Y	FA	Y	Y
11	15/8/2006 04:32	−3.23	2.67	19.24	−0.37	G	Y	FA	N	Y
12	15/8/2006 05:19	−3.47	2.70	18.99	−0.51	G	Y	FA	Y	Y
13	15/8/2006 05:50	−2.62	2.73	18.82	−0.59	G	Y	P	N	N
14	25/8/2006 04:02	−2.00	23.07	45.82	11.61	I	N	–	Y	N
15	7/9/2006 13:12	−2.67	2.17	22.76	1.09	I	N	–	N	N
16	7/9/2006 16:15	−4.56	2.26	21.99	0.76	G	Y	FA	Y	N
17	7/9/2006 16:59	−2.67	2.28	21.84	0.70	G	Y	FA	Y	Y
18	16/9/2006 03:50	−1.08	0.08	36.65	14.32	I	Y	FA	N	Y
19	8/10/2006 07:09	−1.78	1.53	28.07	8.33	G	Y	FA	Y	Y
20	8/10/2006 08:06	−1.47	1.55	27.91	8.16	G	Y	FA	Y	Y
21	9/10/2006 12:48	−2.80	2.16	22.01	1.78	I	Y	FA	Y	Y
22	4/11/2006 06:21	−1.54	1.20	27.97	18.56	I	Y	FA	Y	Y
23	7/12/2009 13:38	−3.09	21.03	25.98	0.30	I	Y	FA	Y	Y
24	18/3/2010 17:06	−1.51	20.89	22.93	0.38	I	N	–	Y	N
25	19/3/2010 21:17	−3.41	22.03	13.91	0.34	I	Y	None	Y	Y
26	25/4/2010 04:57	−1.05	20.52	26.05	0.15	I	N	–	Y	N
27	28/11/2010 06:34	−1.97	20.54	22.54	−0.07	I	Y	FA	N	N

Note. CHEMS = Charge Mass Spectrometer; ELS = electron spectrometer; LEMMS = Low-Energy Magnetospheric Measurement System; CAPS = Cassini Plasma Spectrometer.
[a]FA = Field aligned, P = Perpendicular, None = No structure.

population is limited in vertical (or latitudinal) extent. In addition, the technique used to select the signatures (section 3.2 and Appendix B) requires the presence of a background plasma sheet population with which the heated population can be compared. Therefore, many dipolarization signatures (from the perspective of the magnetic field) may be observed outside of the plasma sheet where the electron counts are too low to result in a CAPS-based detection. The technique is also fairly specific, and it is likely that it is insensitive to some forms of heating that could be displayed.

However, on inspection, $^{475}/_{695}$ events show an average value of $|B_R| \leq 2$ nT during the field deflection, suggesting Cassini was reasonably close to the current sheet and thus the CAPS instrument would have been capable of sampling plasma sheet electrons. Indeed, during the dipolarization presented by Jackman et al. (2013) the current sheet was encountered both shortly before and after the magnetic field signature, suggesting that Cassini should have encountered a latitudinally confined energetic electron population (certainly following the magnetic field deflection). This suggests that either some southward magnetic field deflections and dipolarizations do not result in heated electrons or that the dipolarizing heated electron flux is also limited in azimuthal width.

Table 2
Table Summarizing Several Kronian Dipolarizations From the Literature

	$\lvert\Delta B_\theta\rvert$	Increase in energetic electrons
Bunce et al. (2005)	3.5 nT	Y
Russell et al. (2008)	1.6 nT	N
Jackman et al. (2013)[a]	0.8 nT	N
Thomsen et al. (2013)	3.41 nT/none	Y/N
Thomsen, Jackman, et al. (2015)	0.98 nT	Y
Jackman et al. (2015)	2.4 nT	N

[a]Jackman et al. (2013) discussed three dipolarizations; however, two were previously reported by Bunce et al. (2005) and Russell et al. (2008).

At Earth, the energetic electron flux has been shown to be dependent upon the spacecraft location relative to the dipolarization front; with observations on the duskside of the front showing lower electron flux (Runov et al., 2013). The electron drifts that lead to this asymmetric signature over the front could explain a good fraction of the detections. In addition, terrestrial observations suggest that only magnetic field deflections associated with enhanced dawn-dusk electric fields are associated with energetic particle flux (Gabrielse et al., 2012; Liu et al., 2016). Unfortunately, it is not possible to test this with the data available from Cassini at Saturn.

Yao, Grodent, et al. (2017) recently proposed two drivers of dipolarizations at Saturn, the first of which is the main target of this study: reconnection-driven fronts. The second type, with a similar magnetic field signature is instead attributed to a disruption of the cross-tail current systems. This current disruption, while resulting in a rotation of the field, may not be very efficient at energizing the electron population (Yao, Grodent, et al., 2017). Furthermore, this mechanism would not manifest with a sharp boundary between distinct plasma populations, potentially meaning that these type of events would not selected by our method (Appendix B). Additionally, there are other magnetospheric processes or structures that can result in a sudden tilting of the magnetic field. For example, Alfvénic waves or crossing into different magnetospheric structures can rotate the orientation of the magnetic field. Such structures include the low-latitude boundary layer (Masters et al., 2011) (located near the magnetopause) and the magnetotail plasma sheet (e.g., Jackman et al., 2009).

Moving toward the magnetotail current sheet would have the effect of reducing the value of B_R and increasing n_e. If the 10 min preceding and following the deflection of the field are compared, it is found that only $^{50}/_{695}$ events show a B_R reduction of at least 1 nT coupled with a greater than 10% increase in n_e. This interpretation cannot therefore explain the majority of the MAG detections.

We conclude that the majority of the MAG detections (that lack coincident electron energization signatures) are due to a combination of the relative location of the spacecraft, disruption of the magnetotail current systems, or passages into adjacent magnetospheric structures. The first possibility would suggest that the energetic electron population is much more limited in spatial extent than the magnetic field signature, as is the case at Earth (e.g., Runov et al., 2013). The second suggestion would imply that disruption of the current systems is much more common than reconnection-driven dipolarization fronts, or that the effect covers a wider azimuthal region. More work is needed in the future to distinguish between these possibilities.

4.2. Electron Signatures Lacking a Significant Rotation of the Magnetic Field

In total, 30 ELS detections were made, uncoupled to strong southward field rotations. Energetic electron signatures lacking a corresponding magnetic field signature are often observed at the Earth. At the Earth these signatures are often energy dispersed, suggesting a nonlocal generation mechanism (Duan et al., 2014). It has been suggested that they are due to dipolarization fronts propagating past the spacecraft, dawnward or duskward of the spacecraft position (Gabrielse et al., 2016). However, on inspection of the high-energy electron data available from LEMMS the events in the catalog do not appear to be energy dispersed (given a cadence of 60 s). Therefore, these events could be due to a different phenomenon to those observed at Earth, or the dispersion could be weak (such that the cadence of the data is insufficient). For example, they could be paired with magnetic field rotations that are small relative to background fluctuations of the field (and so do not meet the threshold values used by this work) or lag behind the front to such an extent ($\geq\sim$ 30 min) that it is not possible for the automated method to pair the two. Delayed energetic fluxes have been observed

at the Earth (e.g., Runov et al., 2011). Alternatively, it is possible that the energy dispersion is less apparent at Saturn due to the dominance of corotational motion: the drifts of electrons monitored by LEMMS (i.e., with energies between 20 keV and several MeV) are still largely dominated by corotation. In general, dispersion signatures are rare in this data set beyond ~15 R_S. Gradient/curvature drifts that may cause dispersions would become more apparent toward the upper end of the energy range. Resonant acceleration by wave activity could also result in electron heating.

4.3. Case Study

An example of an event where both a strong magnetic field deflection and energetic electron signature were detected was introduced above in Figure 1. Figures 1f and 1g show the derived electron density and temperature, respectively. Finally, Figure 1h shows the LEMMS energetic electron flux for four energy channels between 18 and 100 keV. The vertical blue and red shaded regions represent those selected by the technique (discussed in section 3.2 and Appendix B) as ambient plasma sheet and energetic population, respectively. The properties of the electron moments within these regions will be explored later, in section 6. During this event Cassini was located at a radial distance of 26 R_S, a local time of 21:00, and a latitude of 0.3°. This represents the earliest local time at which a dipolarization has been observed in situ at Saturn prior to this work.

The combination of magnetic field deflection and electron energy enhancement used to identify the event can be seen in Figures 1b and 1e at around 13:40. Meanwhile, Figures 1f and 1g show that the change in electron spectrogram corresponds to an increase in the electron temperature and a reduction in the density, as is seen in terrestrial dipolarizations (e.g., Runov et al., 2015). This is a feature common to all of the 28 events identified (likely a result of the specificity of the selection method employed) and will be explored in more detail in section 6. Figure 1h shows how the energetic population observed by the ELS instrument (shown in Figure 1e: electrons up to 26 keV) can extend up to several hundred keV. Figure 1h also demonstrates that the increase in energetic electron counts is dispersionless: all energy channels increase within 1 min of each other. This mirrors terrestrial dipolarizations, where the bursts of energetic electrons that accompany dipolarization fronts are often dispersionless (Apatenkov et al., 2007; Duan et al., 2014; Gabrielse et al., 2014). A total of $^{19}/_{28}$ dipolarization fronts show an increase in LEMMS electron counts (Table 1), all of which are dispersionless.

Figure 2a shows all-sky images from the CAPS instrument for the dipolarization in Figure 1. In these all-sky images the center of the circle represents the antisaturnward look direction (radially out from the planet), the inner dashed circle represents directions 90° from this, and the outer edge represents the saturnward direction. The hollow triangle indicates the direction of strict corotation. The flow preceding the dipolarization front (the first two panels) can be seen to be coming from between the antisaturnward and corotational directions and represents a broad inflow. The flow is coming from slightly above the horizontal that can be explained as the spacecraft was below the current sheet (from the sign of B_r in Figure 1a). The broad inflow can be interpreted as a result of the compression of the plasma sheet ahead of the dipolarization front. Following the passage of the front (in the right-hand panel) the flow can be seen to become more collimated. The velocity of the plasma during this interval can be calculated to be ~1,200 km^{-1}, almost 5 times the strict corotational velocity at this radial distance. Therefore, this represents a very energetic period of inflow, many times the ambient flow speed of the plasma (Mcandrews et al., 2009; Thomsen et al., 2013). Unfortunately, the viewing of CAPS is not often in a direction such that inflowing plasma is within the field of view. For this reason it is not possible to examine the flows statistically.

MIMI/INCA (with its large field of view) enables us to observed the PA (α) distribution of H^+ between ~80 and 180° for energies between 5 and 227 keV. The distribution during the event is shown in Figure 2b. Time advances along the x axis while energy increases vertically. Pitch angle contours are labeled and shown in black. Following the passage of the dipolarization front (~13:37 onward), features of an anisotropic PA distribution become apparent for approximately 10 min (three panels). The most consistent feature (across all energies) of the heated dipolarizing flow is a population at approximately $\alpha = 90°$. This is likely a flow anisotropy; however, it is also possible that adiabatic betatron acceleration plays a role in its generation, as the heated flow has moved to a region of higher field strength. The distributions can also be seen to vary with energy, as is observed at the Earth (e.g., Ashour-Abdalla et al., 2011; Birn et al., 2017; Duan et al., 2014; Pan et al., 2014; Runov et al., 2017). For example, at energies above ~90 keV the presence of a field-aligned population becomes apparent; a population that could be generated by Fermi-type acceleration as the length of the flux tubes decreases.

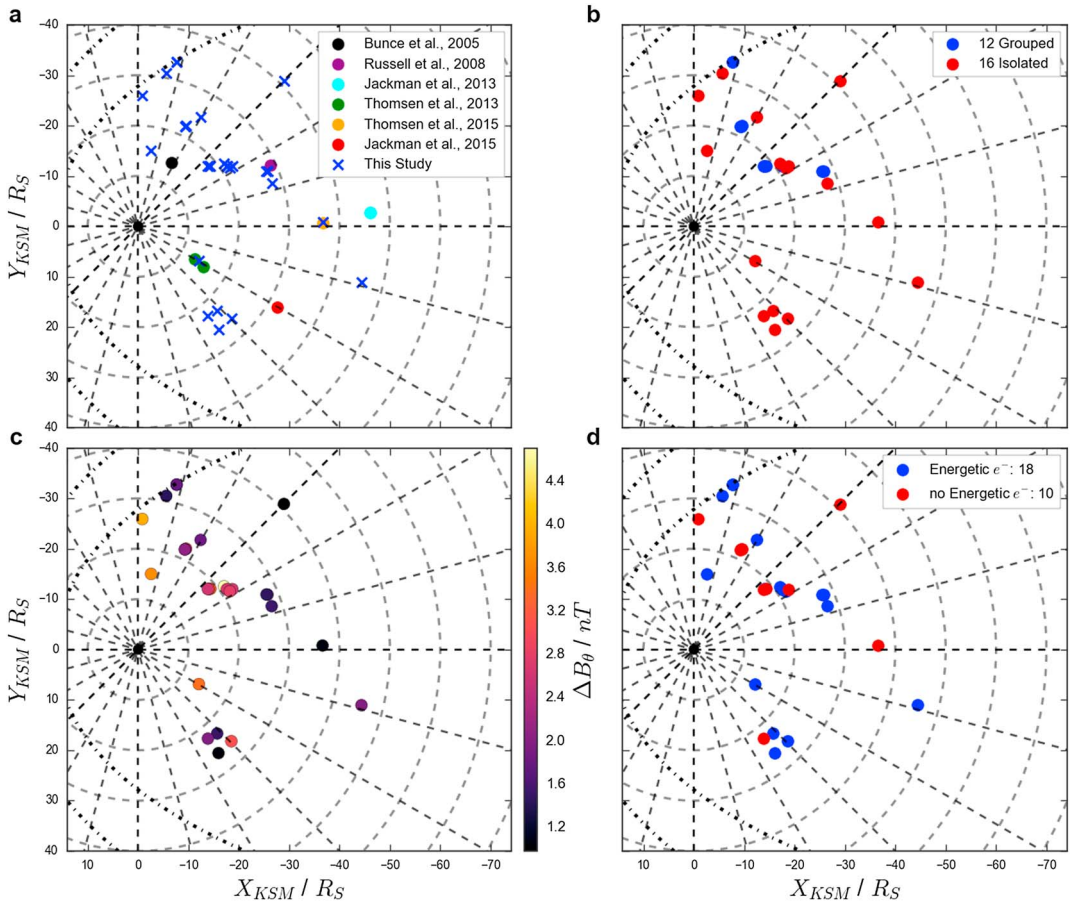

Figure 3. Equatorial projections of Saturn's magnetotail, each hour of local time and every 10 R_S of radial distance are indicated with black dashed lines. The black dash-dotted lines indicate the location of the Kanani and Arridge (2010) magnetopause model for $P_{SW}^{Dynamic} = 0.1$ nPa and 0.01 nPa. Each panel displays the locations of the 28 detections for which both electron energizations and southward magnetic field deflections ($\geq B_\theta^{RMS}$) were observed. (a) The detections from the literature (described in Table 2). (b) The events colored blue if they occur within a group (i.e., within 3 hr of an adjacent event; cf. Jackman et al., 2014; Smith et al., 2016) or red if they are isolated. (c) The events with a color bar according to the size of the magnetic field deflection with which they are associated. (d) The events for which an increase in the Low-Energy Magnetospheric Measurement System ($E_{e^-} \geq 20$ keV) rates are observed (in blue), with the examples for which no increase (or a decrease) are observed (in red).

5. Distribution and Frequency

We now investigate the distribution of the identified events across the Kronian magnetotail. The panels of Figure 3 show the spatial distribution of the 28 events for which both magnetic field deflection and electron energy enhancement were identified.

Figure 3a also includes dipolarizations presented in the literature for comparison. Dipolarizations can be seen to occur across most of the magnetotail, though the majority occur postmidnight ($^{22}/_{28}$). Figure 3b shows the 28 detections highlighted in blue if they occurred within 3 hr of another event (Jackman et al., 2014; Smith et al., 2016) and red if they were isolated. The 3 hr time interval was selected by scaling a 30 min timescale previously used at the Earth (Slavin et al., 1993). Grouped events are solely seen postmidnight, while isolated events are seen across the entire magnetotail. In total, just over half ($^{16}/_{28}$) occur in isolation.

Figure 3c shows how the size of the magnetic field signature varies according to the location of the event. In general, the more distant events from the planet can be seen to possess smaller field deflections. This could be a feature of Kronian dipolarization fronts; however, it could also be a selection effect. In this study the magnetic deflection is required to be greater than a threshold based on the RMS of the field. The meridional field component increases in magnitude as the radial distance decreases: this will result in small field deflections (such as those observed in the deep tail) not being selected at small radial distances. This would be more

consistent with the terrestrial work of Runov et al. (2015), who found that the magnitude of field deflection is fairly invariant with geocentric distance. Alternatively, Ashour-Abdalla et al. (2015) noted in their modeling that dipolarization fronts steepen as they approach the Earth; this could potentially be the Kronian equivalent.

Finally, Figure 3d shows the locations of the events with (blue) and without (red) corresponding increases in LEMMS ($E_{e^-} \geq 20$ keV) count rates. As mentioned in section 4.3, $^{10}/_{28}$ events do not show a simultaneous increase in high-energy electrons, but this does not appear to be an effect of their location: they are spread across the magnetotail with no clear preference. As LEMMS has limited PA coverage, the possibility of anisotropic energetic electron distributions reducing the detection efficiency of the high-energy counterpart of the dipolarizations cannot be excluded, even though Earth-based observations would be more consistent with isotropic energetic electron populations (e.g., Walsh et al., 2011). It is also possible that the energization for these events does not extend beyond the CAPS energy range (above ~26 keV), a possibility if the spacecraft was located closer to the reconnection site during these intervals (and the higher-energy populations are mostly generated by nonlocal mechanisms). If this was the case, it might be expected that the events for which higher T_{e^-} were recorded would be more likely to show increases in LEMMS. Indeed, $^{6}/_{7}$ of the events with the highest T_{e^-} in the dipolarizing material and $^{8}/_{9}$ events with the highest fractional increase in T_{e^-} show increases in LEMMS counts.

6. Plasma Heating

The properties of the hot, tenuous population following the dipolarization front (e.g., that highlighted in red in Figure 1) will now be examined in more detail. Insufficient counts were recorded to analyze the ion populations involved in any of the events, but there were sufficient electron counts to produce usable moments for $^{19}/_{28}$ of the events.

The CAPS/ELS PA spectra were inspected for the 19 events with sufficient electron counts. The PA coverage of CAPS/ELS during these intervals was generally limited to around half of the full 180° distribution. However, all 19 events afforded sufficient coverage to identify when the distributions fell into two broad categories: field aligned (peaking toward 0° or 180°) or perpendicular (peaking around ~90°). In total, $^{18}/_{19}$ events show anisotropic distributions. The vast majority (17 events) showed higher electron fluxes approaching field-aligned orientations; perhaps, suggesting that the majority of the heated low-energy electron population was generated by the (nonlocal) Fermi heating mechanism as the flux tubes contract toward the planet (as has been suggested by Yao, Coates, et al., 2017).

Figures 4a and 4b show density-temperature plots for the electron populations before and after the passage of the dipolarization front, respectively. It should be noted that the spacecraft is not tracking the planetward moving plasma population, and so the "before" measurement is simply taken as representative of the ambient plasma sheet (for the purposes of comparison). Figures 4a and 4b are plotted on the same axes scales for comparison. It can be seen that between the two panels all points move upward and to the left: the electron temperature increase is coupled with a decrease in the density. The colors of the points indicate the radial distance at which the event was encountered. The colors demonstrate that the events furthest from the planet occupy the bottom left of the distribution while those closest to the planet fill the upper right. Runov et al. (2015) performed a similar analysis at the Earth and observed an analogous trend. In general, those dipolarizations observed at greater radial distances are more likely to be closer to the site of reconnection. With a shorter propagation distance, and associated smaller change in field strength, the effects of nonlocal mechanisms (e.g., betatron and Fermi heating) would be smaller in magnitude, as has been found at the Earth (e.g., Birn et al., 2014; Pan et al., 2014; Runov et al., 2015).

Figures 4c and 4d show how the electron temperature and density vary within each event. Figure 4c shows the electron temperature before the front compared to that measured after its passage, while Figure 4d shows the same but for the electron density. The gradients of the linear ($y = mx + c$) least squares fits show that, on average, the temperature increases by between factors 3 and 4, while the density drops by around a factor of 3. The temperature best fit contains a significant constant value (~900 eV). This constant could be interpreted as the minimum temperature increase caused by mechanisms local to the reconnection site (e.g., Fu et al., 2017), though there is also likely a selection effect present: small changes in temperature are less likely to be identified. In addition, the fit is strongly affected by the point that lies to the upper right at $T_e \sim 1$ keV. When this point is excluded from the fit the average fractional temperature change (gradient) increases to a factor of 6.

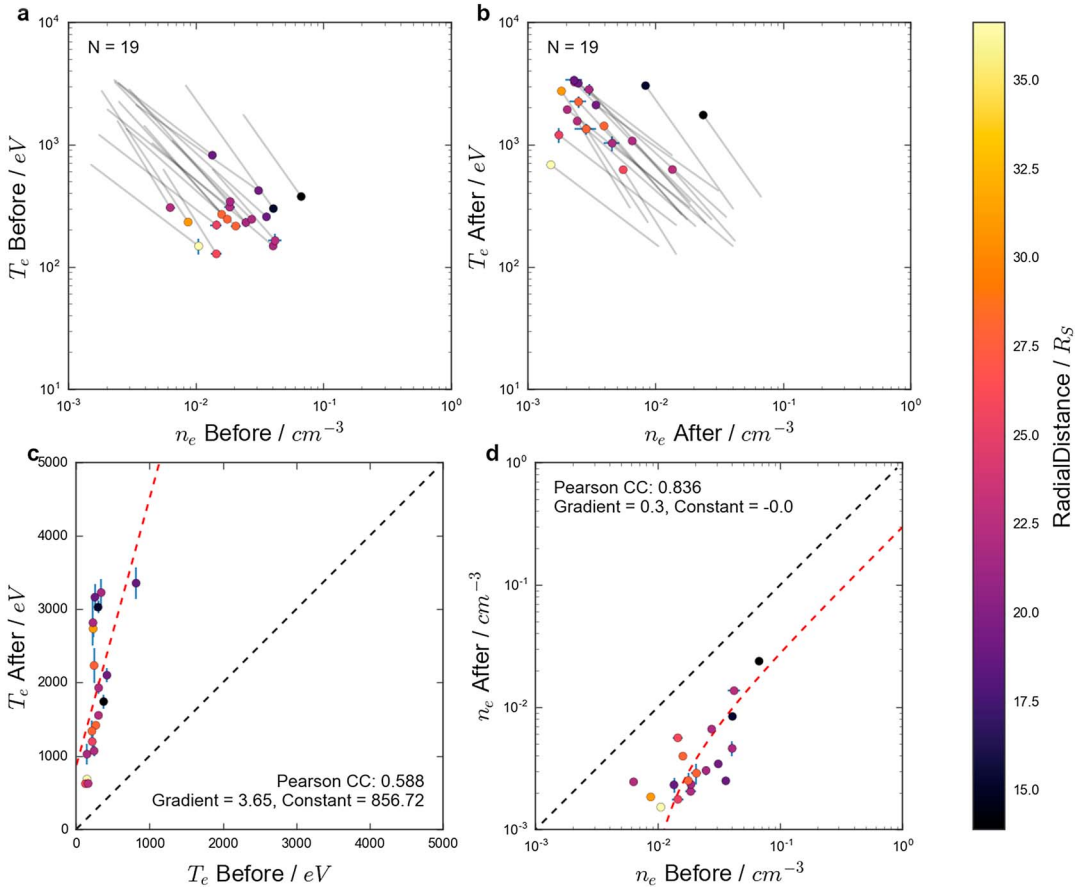

Figure 4. The electron density plotted against the electron temperature for (a) before and (b) after the dipolarization front. These panels are plotted on the same axes scale for direct comparison. The gray lines indicate how the events move in density-temperature space. (c and d) The electron temperature (density) before the front plotted against the electron temperature (density) after the passage of the front. The points and error bars provided are the mean and standard error of the mean, respectively. The diagonal black dashed line shows the location of $y = x$: where the points would lie if there was no change during the passage of the front. The red dashed lines indicate least squares linear fits to the data; the details of the fit parameters are provided on the panels. The color bar for all four panels indicates the radial distance at which the spacecraft encountered the event.

We now explore the changes in electron temperature and density with respect to their location within the magnetotail. Equatorial projections of the magnetotail are shown in Figure 5. The color bar of Figure 5a shows the fractional increase in T_e following the passage of the dipolarization front ($T_e^{\text{After}}/T_e^{\text{Before}}$), while the color bar of Figure 5b shows the fractional change in n_e ($n_e^{\text{After}}/n_e^{\text{Before}}$). The panels only include those events for which sufficient electron moments are available, as above ($19/28$). It should be noted that the fractional temperature increases are almost all larger than the average calculated using the best fit in Figure 4c. This is likely a result of the arbitrary use of a linear fit and the outlier (discussed above).

The events premidnight can be seen to possess relatively small temperature increases (factors of ~4 in Figure 5a) and preserve the greatest fraction of their density (30–40% in Figure 5b), perhaps suggesting that they are observed when the spacecraft is closer to the reconnection site. As discussed above, the further the events have propagated from the reconnection site, the greater the magnitude of nonlocal heating mechanisms. These premidnight dipolarization fronts could be related to the Vasyliunas cycle stretching, as the mass-loaded flux tubes rotate around the dusk flank and are no longer confined by the magnetopause.

In contrast, the events postmidnight show a much greater range of variation of plasma properties: some show very large heating factors (tenfold to twelvefold increase), while others are more similar to those observed premidnight. These observations could be explained by a larger variation in x-line location in the postmidnight region of the magnetotail, with the dipolarizations propagating from different downtail locations.

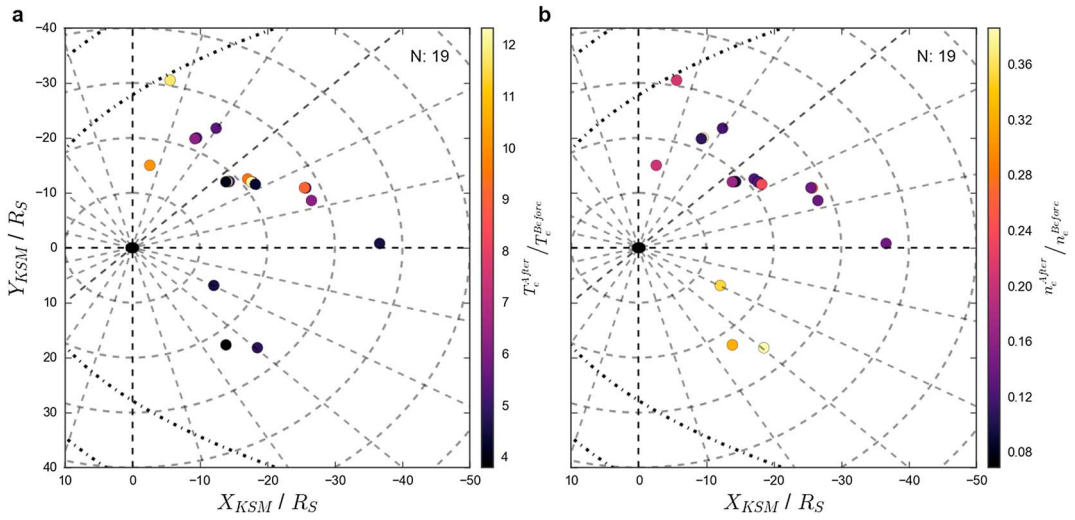

Figure 5. Equatorial projections of Saturn's magnetotail, as in Figure 3. The panels display the 19 events for which electron moments were available both before and after the passage of the front. (a) The fractional temperature change over the event. (b) The fractional change in density.

Experiencing a more significant change in total field strength would explain the greater possible heating observed postmidnight. Additionally, if the distance between the effective mirror points shrinks significantly, then the plasma would be more dramatically heated. Finally, the range of densities measured after the dipolarization also varies from 10% to 30% of that measured within the ambient plasma sheet.

7. Composition

We now explore the dipolarizations with respect to the relative composition of their plasma. In general, the plasma sheet would be expected to be populated by ions of internal magnetospheric origin, comprising both light ions (e.g., H^+ and H_2^+) and heavier water group ions (W^+) from Enceladus (e.g., O^+, OH^+, H_2O^+ and H_3O^+). The presence of species that are more prevalent in the solar wind (e.g., He^{++}) could act as an indication that the reconnection process has involved the closure of open field lines, for example, related to the Dungey cycle. Fortunately, the CHEMS instrument is capable of distinguishing several of the ion species and charge states of interest: for example, He^{++} and H_2^+ (of external and internal origin, respectively). It should be noted that CHEMS measures the composition of the suprathermal ($E \geq\sim 10$ keV) plasma, which may differ from that of the thermal plasma ($E \sim 100$ eV) due to species dependent heating and loss mechanisms.

Figure 6 shows example CHEMS PHA (pulse-height analysis) data. Figure 6a shows the counts ($\sim$10 keV $\leq E \leq$ 236 keV) integrated over an interval of ambient plasma sheet preceding a dipolarization front on day 282 2006, while Figure 6b shows the integrated counts obtained within the heated population following the front. Mass per charge versus mass boxes for specific species of interest are shown, as are the number of counts and their compositional fraction. As mentioned above, He^{++} (marked in red) and H_2^+ (marked in blue) are indistinguishable based solely upon mass per charge histograms (i.e., along the *x* axis and the upper histograms).

For this study, the addition of atomic mass information allows us to unambiguously differentiate internal from external plasma populations. The abundances of He^{++} and W^+ group ions will be compared before and after the passage of the front. In the example shown in Figure 6 it can be seen that the W^+ group fraction drops by a factor of 2 between the intervals. The He^{++} fraction increases slightly but not significantly compared to the change in W^+. H^+ is not directly used as a tracer as it could originate from Saturn's ionosphere, Enceladus, Titan, or the solar wind (Felici et al., 2016; Glocer et al., 2007). Combining the reduction in W^+ with the relatively steady He^{++} suggests that this dipolarization is associated with the release of a plasmoid (unobserved on the tailward/distant side of the reconnection site), in which the heavy W^+ group ions have been preferentially lost (cf. Badman & Cowley, 2007; Thomsen et al., 2013, 2014). If the reconnection had proceeded to involve lobe field, then the He^{++} fraction would have been expected to increase. Also, while the integration times for both

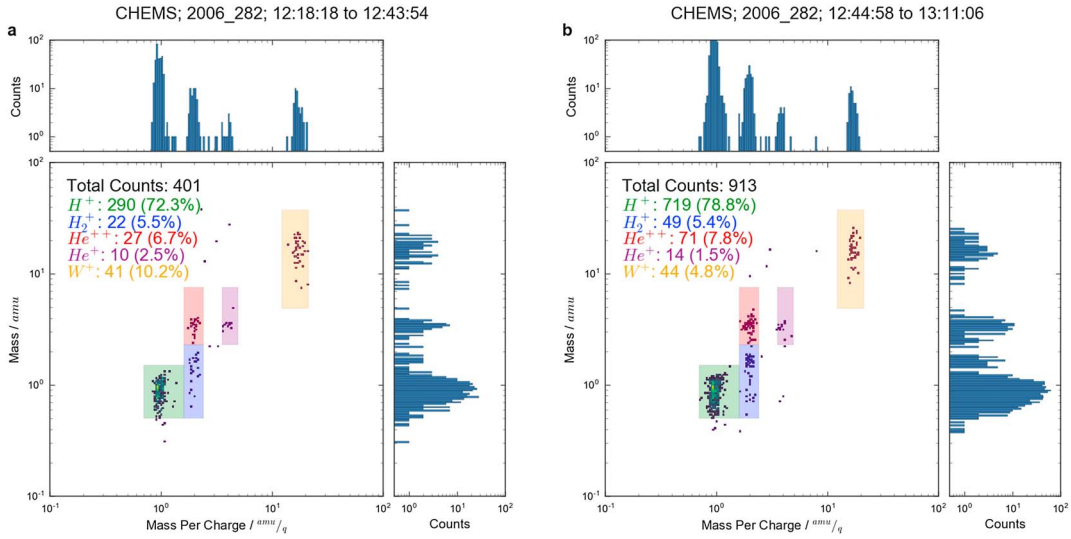

Figure 6. CHEMS PHA (pulse-height analysis) data (a) before the dipolarization and (b) within the heated population following the front on 9 October 2006. Colored boxes are placed on the histogram to indicate the locations of specific species relevant to this study. The corresponding counts and fractional compositions are displayed in the upper left of each panel.

panels are similar (~26 min) the counts in the second interval are much higher, providing additional evidence that significant heating has occurred.

Figure 7 explores the composition of the dipolarizations statistically, showing equatorial projections of the magnetotail. Figure 7 shows the 15 dipolarizations that provided sufficient CHEMS counts (≥30) both before and after the dipolarization front. Sufficient counts were required in both intervals as the scale height has been found to vary for different ion species in the plasma sheet (Kellett et al., 2009; Sergis et al., 2011); motion of the plasma sheet could change the composition and so the comparison must be made with immediately adjacent material. Figures 7a, 7c, 7e, and 7g show the relative abundances measured before the passage of the front, while Figures 7b, 7d, 7f, and 7h show the fractional changes in those abundances measured within the dipolarizing material (i.e., a value of two would indicate a doubling in fractional abundance). The events displayed in the right-hand panel are plotted in gray if the change was not statistically significant (at the $p = 0.1$ level). Therefore, red indicates significant decreases in the fractional abundance/ratio, while blue shows a large increase.

Figure 7a shows the W^+ group fraction before the passage of the dipolarization front. A large range in water group fraction is observed, with fractions ranging between ~0% and 40%. Figure 7b then shows the relative change in % W^+ within the dipolarizing material relative to the previous panel. Just under half of the events ($^6/_{15}$) show a significant depletion of W^+ relative to the preceding ambient plasma sheet. This could either be as a result of the reconnection of lobe field or the preferential loss of equatorial heavy W^+ ions in departing plasmoids (e.g., Badman & Cowley, 2007; Thomsen et al., 2013, 2014). Two events display a significant increase in W^+ fraction.

Similarly, Figures 7c and 7d show the He^{++} fraction in the ambient plasma sheet and the relative change within the dipolarizing material. It can be seen that the He^{++} fraction is, in general, much smaller than the W^+ group fraction. The ambient plasma sheet (Figure 7c) generally contains less than 5% He^{++}, with only one interval recording a higher fraction than this. One event, located ~35 R_S down the tail at midnight, shows a strong increase from 2% to 13% He^{++} (saturating the color bar in 7d). Such an increase suggests that perhaps open field lines have been closed during this event, leading to the inclusion of more plasma of solar wind origin. The vast majority of events ($^{13}/_{15}$) show no significant change in He^{++}%. This is likely related to the small number of He^{++} counts generally recorded (and the resulting large statistical uncertainties).

Figures 7e–7h investigate the ratios of several light ion species and their relative changes. These light ion ratios should be insensitive to plasmoid release (unlike the more equatorially confined W^+ group) and thus provide another indicator of potential Dungey-style reconnection. H_2^+ has an internal source, and thus, it could

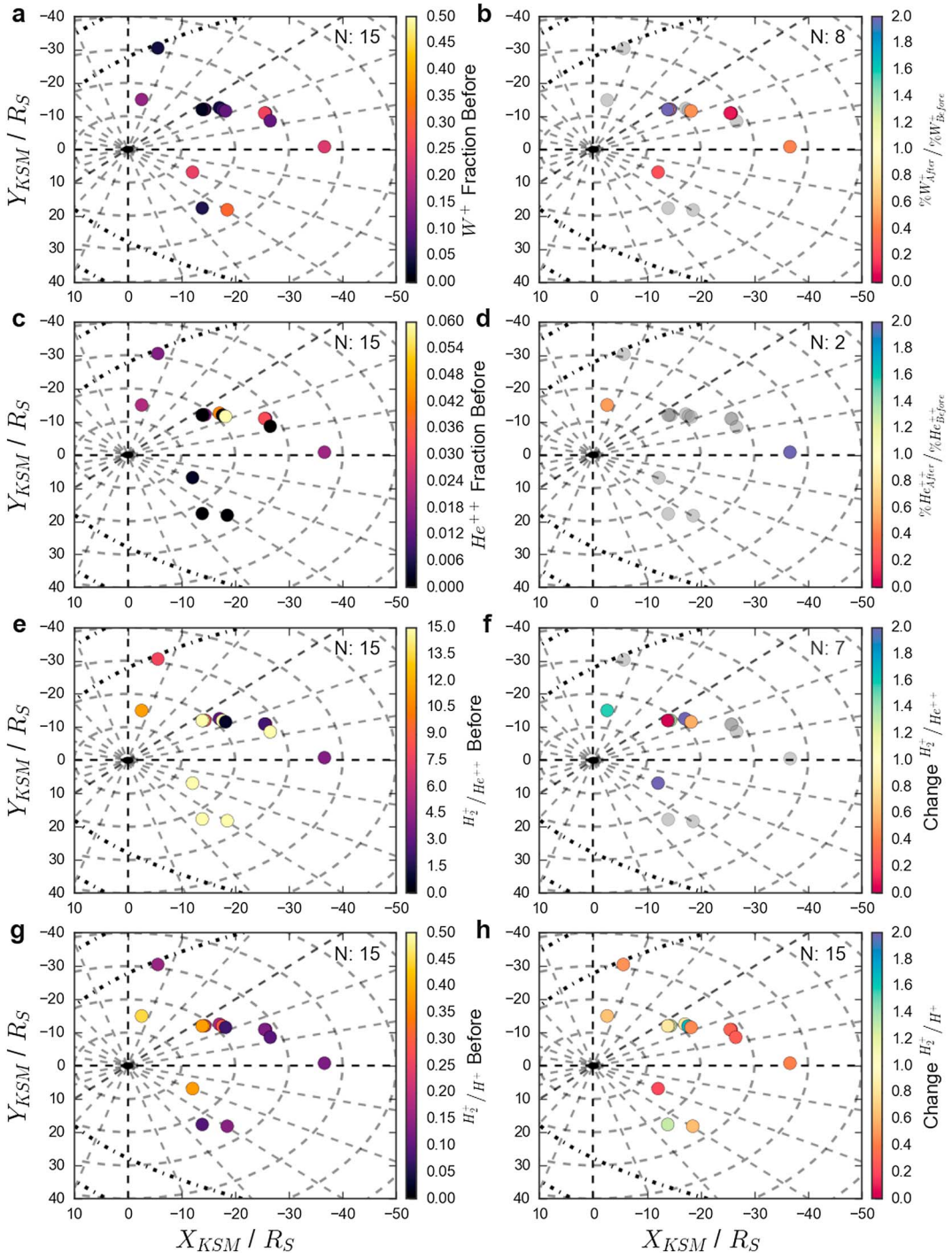

Figure 7. Equatorial projections of Saturn's magnetotail, as in Figures 3 and 5. The panels display the 15 events for which sufficient CHEMS counts (≥30) were collected in both the background and heated populations. The fractional population of (a) W^+ and (c) He^{++} observed before the passage of the front. (b and d) The change in W^+ and He^{++} fractions observed in the dipolarizing material relative to the background (Figures 7a and 7c): blue/green indicates the fraction has increased while red/orange indicates a reduction. The ratios of (e) $^{H_2^+}/_{He^{++}}$ and (g) $^{H_2^+}/_{H^+}$ before the front. (f and h) The relative change in the ratios within the dipolarizing material.

be illuminating to compare its abundance to He^{++}. Figures 7e and 7f show the ratios of $^{H_2^+}/_{He^{++}}$ before the passage of the front and the relative change within the dipolarizing material. A decrease in the $^{H_2^+}/_{He^{++}}$ fraction, coupled with a depletion of W^+, and increase in He^{++} would be conclusively indicative of Dungey-type lobe reconnection. Figure 7f does highlight one event for which the ratio decreases (which also displayed a strong reduction in W^+ in Figure 7b). This event is located postmidnight at ~20 R_S and a local time of 0200.

Unfortunately, the ratio of H_2^+ and He^{++} is statistically insignificant (at the $p = 0.1$ level) for $^8/_{15}$ events, likely due to the sparsity of He^{++}. For this reason Figures 7g and 7h investigate the ratio of H_2^+ to H^+. While H^+ (and therefore this ratio) is not a decisive diagnostic of external/lobe involvement (as it has both internal and external sources) a relative increase in its abundance (compared to H_2^+) combined with other significant changes in the panels above (e.g., a significant decrease in W^+) would be suggestive of lobe involvement. Likely due to the large numbers of counts in both species, all 15 events show significant ($p \leq 0.1$) changes in Figure 7h. Both events highlighted above (located at 35 R_S and 20 R_S) show strong decreases in this ratio, building on the evidence of the above panels. These two events are located fairly deep in the tail or postmidnight. It has been suggested that reconnection cannot proceed onto open field lines until the flux tubes have rotated past midnight (e.g., Thomsen et al., 2013), consistent with this result.

The complete absence of W^+ group ions would not necessarily be expected from a dipolarization resulting from Dungey-type reconnection of open field lines, even assuming that "pure lobe" reconnection is possible. Thomsen, Jackman, et al. (2015) argue that some W^+ can originate in the mantle and be subsequently involved in lobe reconnection. Additionally, a combination of terrestrial work and modeling has suggested that plasma from the adjacent plasma sheet becomes entrained in the reconnection outflow (Eastwood et al., 2015). This mechanism would also suggest that Dungey-type dipolarizations that have propagated from deep within the tail would be expected to contain significant W^+ accumulated during their propagation. For these reasons the presence of W^+ is not a decisive indicator of purely Vasyliunas-type reconnection.

8. Conclusions

Analysis of dipolarization fronts within Saturn's magnetotail has been presented. Southward deflections of the magnetic field were first identified, as were intervals where an energized electron population was present. In total, 28 events with clear signatures in both the magnetic field and CAPS ELS data have been analyzed. The vast majority of significant southward field rotations (≥95%) were unaccompanied by the required change in electron population, while 48% of identified electron signatures were coincident with large rotations of the field. The large number of southward field deflections not coincident with significant changes in the electron energy distribution could be due to the spacecraft's location relative to the current sheet, inefficient heating from disruption of cross-tail current systems, or changes in the spacecraft's magnetospheric environment.

An example dipolarization (showing terrestrial-like properties) was presented displaying a strong southward field rotation coupled with a reduction in the density and a heating of the electron population. The high-energy electron counts increased in a dispersionless fashion following the passage of the front. The direction and speed of plasma flow were found to be planetward and around 5 times the corotational velocity. The pitch angle spectra show significant counts in both the perpendicular and field-aligned orientations, which can be explained by flow anisotropies and the nonlocal betatron and Fermi mechanisms heating the plasma during its planetward passage.

Dipolarizations were identified over the majority of the magnetotail, but most were located postmidnight ($^{22}/_{28}$). Several chains of dipolarizations were observed (a chain defined as multiple events, each separated by less than 3 hr). These chains of dipolarizations were solely observed postmidnight. The dipolarizations observed furthest from the planet were found to possess smaller deflections of the magnetic field, while the largest deflections were identified closest to the planet. This is likely a selection effect, as the threshold deflection size increases at smaller radial distances (corresponding to the stronger meridional field component).

The majority of the low-energy ($E \leq 26$ keV) dipolarizing electron populations were found to have large relative fluxes in the field-aligned orientations, possibly as the result of Fermi-type heating mechanisms. The electron temperature and density were found to be anticorrelated following the passage of the dipolarization front. The electron temperature increased by factors of around 6, while the density dropped by a factor of approximately 3. Premidnight dipolarizations were found to be accompanied by the smallest relative heating

and density depletions, while those postmidnight displayed a much larger range of temperature and density variation. This could perhaps be explained by a more consistent x-line forming closer to the planet premidnight, while postmidnight the location of the x-line varies over a much larger range of radial distances. If this was the case, then postmidnight the dipolarizing material could travel over larger distances, increasing the magnitude of nonlocal heating effects.

The composition of the heated dipolarizing flows was compared to that of the adjacent ambient plasma sheet. Six of the events (40%) show significant ($p \leq 0.1$) reductions in W^+ group fraction, which could be caused by the preferential loss of equatorial heavy ions in departing plasmoids or the closure of open field lines. Two of these events also show other compositional changes suggestive of the reconnection of open field lines.

Appendix A: Event Selection: Magnetic Field Deflection

In this appendix, we summarize the method by which meridional magnetic field deflections are identified. The method is described in comprehensive detail by Smith et al. (2016).

First, a running average of the B_θ component of the field is calculated using a 1 hr sliding window. Instances where this running average passes through the data are listed and will be referred to as "crossings." In general, crossings can be considered to be loci located somewhere along a field deflection, that is, between local peaks of the field. For each crossing the local maxima and minima are identified on either side, within a 20 min window. The orientation of the crossing dictates on which side the maxima or minima are selected as appropriate. All possible combinations of the maxima and minima are paired together, and second-order polynomials are fit to the resulting data between each pair. The quality of the fit between the polynomials and the data is then calculated (using the coefficient of determination: r^2); if it is greater than an empirical threshold ($r^2 \geq 0.9$), then the fit is provisionally selected. Finally, the pair of maxima and minima for which the value of $|\Delta B_\theta|$ (the absolute size of the magnetic field deflection) is greatest is selected. This value of $|\Delta B_\theta|$ can then be compared to the local RMS of the field: B_θ^{RMS} (calculated for a 1 hr window centered on the crossing) and rejected if deemed too small. Smith et al. (2016) placed a lower limit of $1.5B_\theta^{\mathrm{RMS}}$.

Appendix B: Event Selection: Electron Energy Enhancement

In this appendix we describe a method developed to identify the arc-like signature of energized electrons highlighted in Figure 1e. The method is model independent and could be of use in identifying other magnetospheric phenomena.

Two spectra can be compared using quantile-quantile (QQ) plots (Gilchrist, 2000). This technique allows the direct comparison of two distributions without requiring a specific model to be chosen. In the past it has been applied to solar wind data in order to investigate the variation in several parameters over the solar cycle (Tindale & Chapman, 2016). Figure B1 shows the result of comparing two spectra (from the event in Figure 1) with the technique. Figure B1a shows the magnetic field for a 1 hr window surrounding a significant southward magnetic field deflection (increase in B_θ). The ELS flux spectrogram for the same interval is shown in Figure B1b.

The two example spectra chosen for comparison are shown in Figure B1c. The blue distribution is taken within the plasma sheet population (before the dipolarization magnetic signature), while the red is taken within the heated electron population. Each spectrum is first converted into a cumulative distribution function (CDF: C), where $C(x)$ is the probability that the value of the variable $\tilde{x}$ is less than or equal to x ($\tilde{x} \leq x$). Inverting the CDF (creating the iCDF: C^{-1}) provides a method of inferring the energy of the distribution at a given probability.

Two iCDF distributions can then be directly compared, plotting C_1^{-1} against C_2^{-1}; each point then shows the energy of each distribution for a given probability. This is known as a QQ or quantile-quantile plot; an example of which can be seen in Figure B1d. If the two distributions are identical ($C_1^{-1} = C_2^{-1}$), then the QQ plot will lie on the line of $y = x$ (the black dashed line in Figure B1d). This study concerns the change in plasma distribution during the dipolarization: the difference between the QQ plot and $y = x$.

The characteristic "*S*" shape shown in Figure B1d shows that the spectrum before the dipolarization signature has a larger flux at lower energies (i.e., below around 500 eV), while the spectrum taken after the signature is concentrated at higher energies with a relative loss of the lower-energy counts. This technique has been

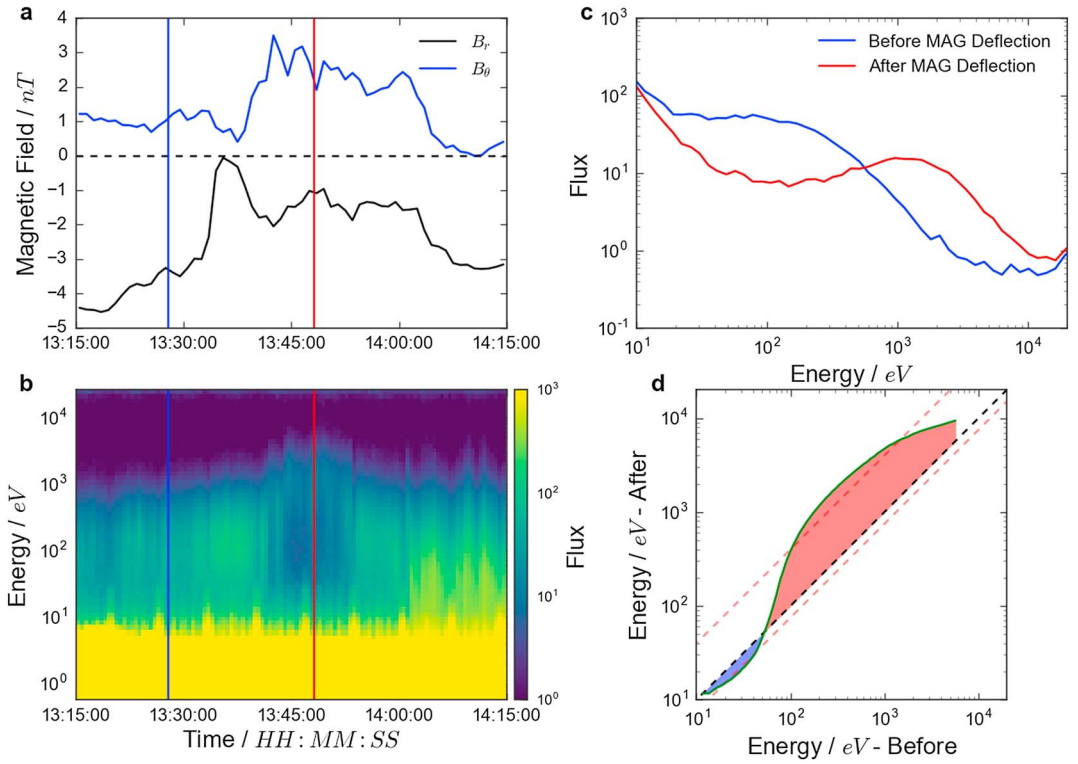

Figure B1. Figure demonstrating a quantile-quantile (QQ) statistical comparison. (a) The B_r (black) and B_θ (blue) components of the magnetic field for 1 hr surrounding the example dipolarization from Figure 1. (b) The corresponding electron flux spectrogram around this interval. The vertical red and blue lines in Figures B1a and B1b indicate the times of two spectra that have been selected and are shown in Figure B1c. (d) The resulting QQ plot of the comparison between the two spectra, the black dashed line indicates $y = x$: where the plot would be should the spectra be identical. Regions above (below) $y = x$ have been shaded red (blue). The diagonal red dashed lines indicate the empirical thresholds.

specifically designed to search for this type of shift in spectrum based on terrestrial work (Deng et al., 2010; Pan et al., 2014; Runov et al., 2013). This signature is common to all previously identified Kronian dipolarizations (which are associated with electron acceleration).

In order to check for this signature the method uses the diagonal red dashed lines in Figure B1d, corresponding to $y = 4x$ and $y = 0.75x$. These represent empirical limits required to show strong deviation from the $y = x$ line, that is, that the populations are significantly different. The limits have been empirically tuned to select those spectra that show the desired characteristic change in electron population. If both diagonal lines are crossed by the QQ curve, then the technique reports that the signature of interest has occurred, subject to the following checks.

1. There are only two changes in the population, that is, a single clear *S* shape is seen.
2. The *S* shape has the correct orientation: the increase in counts following the magnetic detection is at a higher energy than the dropout.
3. The crossover between the populations occurs between 50 eV and 2 keV (i.e., where the QQ plot crosses through $y = x$).

These criteria were developed from the inspection of trial events (e.g., Bunce et al., 2005; Thomsen et al., 2013), and attempts to reproduce the spectra may have been chosen by eye. Physically, criterion 1 suggests there must be a simple change in the location of the majority of the population (a shift in energies). Criterion 2 requires that the shift must be to higher energies. Finally, criterion 3 requires that the change must be from the typical plasma sheet population to something more energetic (i.e., it must not solely be a small increase in counts at the very top of the energy spectrum).

To apply this method to the data set, a sliding comparison is performed. Every other spectrum (to minimize computational time) is compared to those spectra spaced between 9 and 30 min ahead. If the comparison

flags that the characteristic shift in the spectrum has occurred, then the interval is logged. The comparison is applied to the full data set (described in section 2), and then the logged intervals are grouped into regions of "background" (grouping the catalog of initial spectra) and "heated" (grouping the catalog of "energized" spectra) populations. The grouping is automated, with the following procedure.

In an interval the first lower-energy spectra is tagged as background. All identified spectra are then iterated through in chronological order. Subsequent lower-energy spectra are grouped into the background category until a higher-energy spectrum is encountered. In this manner periods of up to 30 min preceding the heated population can be classified as background.

The detections made by the technique are then checked by eye to ensure they represent the phenomenon of interest. The majority of false detections from this method were the result of the presence of anisotropic electron distributions. Additionally, to reduce false detections the spectra were truncated at both low ($\leq$10 eV) and high energies ($\geq$20 keV). The low energies are dominated by spacecraft photoelectrons, while the high energies can be affected by the efficiencies used to correct the data (occasionally magnifying background noise) (cf. Thomsen et al., 2016).

Acknowledgments
Part of this work was discussed within the ISSI team on How does the Solar Wind Influence the Giant Planet Magnetospheres? A. W. S. thanks M. K. Dougherty for access to Cassini Magnetometer data, and S. Kellock and L. Alconcel at Imperial College London for MAG data processing. Cassini MAG data processing activities are supported in the United Kingdom by STFC. A. W. S. thanks A. J. Coates and G. R. Lewis for CAPS/ELS moments processing. A. W. S. is funded by a SEPnet PhD studentship. C. M. J. is supported by a Science and Technology Facilities Council Ernest Rutherford FellowshipST/L004399/1. M. F. T. is supported by the NASA Cassini program through JPL contract 1243218 with Southwest Research Institute. The magnetic field, CAPS (including moments), and LEMMS data shown in this analysis are available from the Planetary Data System (http://pds.nasa.gov/). A. W. S. would like to thank A. Masters, C. S. Arridge. and P. A. Delamere for helpful discussions. Data analysis and plotting were conducted in Python. Specifically, the libraries used were NumPy, SciPy, Matplotlib, and Pandas.

References

Angelopoulos, V., Baumjohann, W., Kennel, C. F., Coroniti, F. V., Kivelson, M. G., Pellat, R., et al. (1992). Bursty bulk flows in the inner central plasma sheet. *Journal of Geophysical Research*, *97*(A4), 4027–4039. https://doi.org/10.1029/91JA02701

Angelopoulos, V., Coroniti, F. V., Kennel, C. F., Kivelson, M. G., Walker, R. J., Russell, C. T., et al. (1996). Multipoint analysis of a bursty bulk flow event on April 11, 1985. *Journal of Geophysical Research*, *101*(A3), 4967–4989. https://doi.org/10.1029/95JA02722

Angelopoulos, V., Kennel, C. F., Coroniti, F. V., Pellat, R., Kivelson, M. G., Walker, R. J., et al. (1994). Statistical characteristics of bursty bulk flow events. *Journal of Geophysical Research*, *99*(A11), 21,257–21,280. https://doi.org/10.1029/94JA01263

Apatenkov, S. V., Sergeev, V. A., Kubyshkina, M. V., Nakamura, R., Baumjohann, W., Runov, A., et al. (2007). Multi-spacecraft observation of plasma dipolarization/injection in the inner magnetosphere. *Annales de Geophysique*, *25*(3), 801–814. https://doi.org/10.5194/angeo-25-801-2007

Arridge, C. S., André, N., McAndrews, H. J., Bunce, E. J., Burger, M. H., Hansen, K. C., et al. (2011). Mapping magnetospheric equatorial regions at Saturn from Cassini prime mission observations. *Space Science Reviews*, *164*(1–4), 1–83. https://doi.org/10.1007/s11214-011-9850-4

Arridge, C. S., Gilbert, L. K., Lewis, G. R., Sittler, E. C., Jones, G. H., Kataria, D. O., et al. (2009). The effect of spacecraft radiation sources on electron moments from the Cassini CAPS electron spectrometer. *Planetary and Space Science*, *57*(7), 854–869. https://doi.org/10.1016/j.pss.2009.02.011

Arridge, C. S., McAndrews, H. J., Jackman, C. M., Forsyth, C., Walsh, A. P., Sittler, E. C., et al. (2009). Plasma electrons in Saturn's magnetotail: Structure, distribution and energisation. *Planetary and Space Science*, *57*(14–15), 2032–2047. https://doi.org/10.1016/j.pss.2009.09.007

Asano, Y., Shinohara, I., Retinò, A., Daly, P. W., Kronberg, E. A., Takada, T., et al. (2010). Electron acceleration signatures in the magnetotail associated with substorms. *Journal of Geophysical Research*, *115*, A05215. https://doi.org/10.1029/2009JA014587

Ashour-Abdalla, M., El-Alaoui, M., Goldstein, M. L., Zhou, M., Schriver, D., Richard, R., et al. (2011). Observations and simulations of non-local acceleration of electrons in magnetotail magnetic reconnection events. *Nature Physics*, *7*(4), 360–365. https://doi.org/10.1038/nphys1903

Ashour-Abdalla, M., Lapenta, G., Walker, R. J., El-Alaoui, M., & Liang, H. (2015). Multiscale study of electron energization during unsteady reconnection events. *Journal of Geophysical Research: Space Physics*, *120*, 4784–4799. https://doi.org/10.1002/2014JA020316

Badman, S. V., & Cowley, S. W. H. (2007). Significance of Dungey-cycle flows in Jupiter's and Saturn's magnetospheres, and their identification on closed equatorial field lines. *Annales Geophysicae*, *25*(4), 941–951. https://doi.org/10.5194/angeo-25-941-2007

Baumjohann, W., Paschmann, G., & Lühr, H. (1990). Characteristics of high-speed ion flows in the plasma sheet. *Journal of Geophysical Research*, *95*(A4), 3801–3809. https://doi.org/10.1029/JA095iA04p03801

Birn, J., Runov, A., & Hesse, M. (2014). Energetic electrons in dipolarization events: Spatial properties and anisotropy. *Journal of Geophysical Research: Space Physics*, *119*, 3604–3616. https://doi.org/10.1002/2013JA019738

Birn, J., Runov, A., & Zhou, X. Z. (2017). Ion velocity distributions in dipolarization events: Distributions in the central plasma sheet. *Journal of Geophysical Research: Space Physics*, *122*, 8014–8025. https://doi.org/10.1002/2017JA024230

Bunce, E. J., Cowley, S. W. H., Wright, D. M., Coates, A. J., Dougherty, M. K., Krupp, N., et al. (2005). In situ observations of a solar wind compression-induced hot plasma injection in Saturn's tail. *Geophysical Research Letters*, *32*, L20S04. https://doi.org/10.1029/2005GL022888

Cao, J. B., Ma, Y. D., Parks, G., Reme, H., Dandouras, I., Nakamura, R., et al. (2006). Joint observations by Cluster satellites of bursty bulk flows in the magnetotail. *Journal of Geophysical Research*, *111*, A04206. https://doi.org/10.1029/2005JA011322

Delamere, P. A., Bagenal, F., Paranicas, C., Masters, A., Radioti, A., Bonfond, B., et al. (2015). Solar wind and internally driven dynamics: Influences on magnetodiscs and auroral responses. *Space Science Reviews*, *187*(1–4), 51–97. https://doi.org/10.1007/s11214-014-0075-1

Deng, X., Ashour-Abdalla, M., Zhou, M., Walker, R., El-Alaoui, M., Angelopoulos, V., et al. (2010). Wave and particle characteristics of earthward electron injections associated with dipolarization fronts. *Journal of Geophysical Research*, *115*, A09225. https://doi.org/10.1029/2009JA015107

Desroche, M., Bagenal, F., Delamere, P. A., & Erkaev, N. (2013). Conditions at the magnetopause of Saturn and implications for the solar wind interaction. *Journal of Geophysical Research: Space Physics*, *118*, 3087–3095. https://doi.org/10.1002/jgra.50294

Dougherty, M. K., Kellock, S., Southwood, D. J., Balogh, A., Smith, E. J., Tsurutani, B. T., et al. (2004). The Cassini magnetic field investigation. *Space Science Reviews*, *114*(1–4), 331–383.

Duan, A. Y., Cao, J. B., Dunlop, M., & Wang, Z. Q. (2014). Energetic electron bursts in the plasma sheet and their relation with BBFs. *Journal of Geophysical Research: Space Physics*, *119*, 8902–8915. https://doi.org/10.1002/2014JA020169

Dungey, J. (1961). Interplanetary magnetic field and the auroral zones. *Physical Review Letters*, *6*, 47–48. https://doi.org/10.1103/PhysRevLett.6.47

Eastwood, J. P., Goldman, M. V., Hietala, H., Newman, D. L., Mistry, R., & Lapenta, G. (2015). Ion reflection and acceleration near magnetotail dipolarization fronts associated with magnetic reconnection. *Journal of Geophysical Research: Space Physics*, *120*, 511–525. https://doi.org/10.1002/2014JA020516

Egedal, J., Fox, W., Katz, N., Porkolab, M., Øieroset, M., Lin, R. P., et al. (2008). Evidence and theory for trapped electrons in guide field magnetotail reconnection. *Journal of Geophysical Research*, *113*, A12207. https://doi.org/10.1029/2008JA013520

Felici, M., Arridge, C. S., Coates, A. J., Badman, S. V., Dougherty, M. K., Jackman, C. M., et al. (2016). Cassini observations of ionospheric plasma in Saturn's magnetotail lobes. *Journal of Geophysical Research: Space Physics*, *121*, 338–357. https://doi.org/10.1002/2015JA021648

Fu, H. S., Cao, J. B., Khotyaintsev, Y. V., Sitnov, M. I., Runov, A., Fu, S. Y., et al. (2013). Dipolarization fronts as a consequence of transient reconnection: In situ evidence. *Geophysical Research Letters*, *40*, 6023–6027. https://doi.org/10.1002/2013GL058620

Fu, H. S., Vaivads, A., Khotyaintsev, Y. V., André, M., Cao, J. B., Olshevsky, V., et al. (2017). Intermittent energy dissipation by turbulent reconnection. *Geophysical Research Letters*, *44*, 37–43. https://doi.org/10.1002/2016GL071787

Fuselier, S. A., Frahm, R., Lewis, W. S., Masters, A., Mukherjee, J., Petrinec, S. M., & Sillanpaa, I. J. (2014). The location of magnetic reconnection at Saturn's magnetopause: A comparison with Earth. *Journal of Geophysical Research: Space Physics*, *119*, 2563–2578. https://doi.org/10.1002/2013JA019684

Gabrielse, C., Angelopoulos, V., Harris, C., Artemyev, A., Kepko, L., & Runov, A. (2017). Extensive electron transport and energization via multiple, localized dipolarizing flux bundles. *Journal of Geophysical Research: Space Physics*, *122*, 5059–5076. https://doi.org/10.1002/2017JA023981

Gabrielse, C., Angelopoulos, V., Runov, A., & Turner, D. L. (2012). The effects of transient, localized electric fields on equatorial electron acceleration and transport toward the inner magnetosphere. *Journal of Geophysical Research*, *117*, A10213. https://doi.org/10.1029/2012JA017873

Gabrielse, C., Angelopoulos, V., Runov, A., & Turner, D. L. (2014). Statistical characteristics of particle injections throughout the equatorial magnetotail. *Journal of Geophysical Research: Space Physics*, *119*, 2512–2535. https://doi.org/10.1002/2013JA019638

Gabrielse, C., Harris, C., Angelopoulos, V., Artemyev, A., & Runov, A. (2016). The role of localized inductive electric fields in electron injections around dipolarizing flux bundles. *Journal of Geophysical Research: Space Physics*, *121*, 9560–9585. https://doi.org/10.1002/2016JA023061

Gilchrist, W. G. (2000). *Statistical modelling with quantile functions*. Taylor & Francis Group. Retrieved from https://books.google.co.uk/books?id=yuZQmAEACAAJ

Glocer, A., Gombosi, T. I., Toth, G., Hansen, K. C., Ridley, A. J., & Nagy, A. (2007). Polar wind outflow model: Saturn results. *Journal of Geophysical Research*, *112*, A01304. https://doi.org/10.1029/2006JA011755

Grigorenko, E. E., Kronberg, E. A., & Daly, P. W. (2017). Heating and acceleration of charged particles during magnetic dipolarizations. *Cosmic Research*, *55*(1), 57–66. https://doi.org/10.1134/S0010952517010063

Huang, S. Y., Fu, H. S., Yuan, Z. G., Zhou, M., Fu, S., Deng, X. H., et al. (2015). Electromagnetic energy conversion at dipolarization fronts: Multispacecraft results. *Journal of Geophysical Research: Space Physics*, *120*, 4496–4502. https://doi.org/10.1002/2015JA021083

Huang, S. Y., Zhou, M., Deng, X. H., Yuan, Z. G., Pang, Y., Wei, Q., et al. (2012). Kinetic structure and wave properties associated with sharp dipolarization front observed by Cluster. *Annales Geophysicae*, *30*(1), 97–107. https://doi.org/10.5194/angeo-30-97-2012

Hwang, K. J., Goldstein, M. L., Lee, E., & Pickett, J. S. (2011). Cluster observations of multiple dipolarization fronts. *Journal of Geophysical Research*, *116*, A00I32. https://doi.org/10.1029/2010JA015742

Jackman, C. M., Achilleos, N., Cowley, S. W. H., Bunce, E. J., Radioti, A., Grodent, D., et al. (2013). Auroral counterpart of magnetic field dipolarizations in Saturn's tail. *Planetary and Space Science*, *82–83*, 34–42. https://doi.org/10.1016/j.pss.2013.03.010

Jackman, C. M., Arridge, C. S., McAndrews, H. J., Henderson, M. G., & Wilson, R. J. (2009). Northward field excursions in Saturn's magnetotail and their relationship to magnetospheric periodicities. *Geophysical Research Letters*, *36*, L16101. https://doi.org/10.1029/2009GL039149

Jackman, C. M., Slavin, J. A., Kivelson, M. G., Southwood, D. J., Achilleos, N., Thomsen, M. F., et al. (2014). Saturn's dynamic magnetotail: A comprehensive magnetic field and plasma survey of plasmoids and traveling compression regions and their role in global magnetospheric dynamics. *Journal of Geophysical Research: Space Physics*, *119*, 5465–5494. https://doi.org/10.1002/2013JA019388

Jackman, C. M., Thomsen, M. F., Mitchell, D. G., Sergis, N., Arridge, C. S., Felici, M., et al. (2015). Field dipolarization in Saturn's magnetotail with planetward ion flows and energetic particle flow bursts: Evidence of quasi-steady reconnection. *Journal of Geophysical Research: Space Physics*, *120*, 3603–3617. https://doi.org/10.1002/2015JA020995

Jasinski, J. M., Arridge, C. S., Lamy, L., Leisner, J. S., Thomsen, M. F., Mitchell, D. G., et al. (2014). Cusp observation at Saturn's high-latitude magnetosphere by the Cassini spacecraft. *Geophysical Research Letters*, *41*, 1382–1388. https://doi.org/10.1002/2014GL059319

Jasinski, J. M., Slavin, J. A., Arridge, C. S., Poh, G., Jia, X., Sergis, N., et al. (2016). Flux transfer event observation at Saturn's dayside magnetopause by the Cassini spacecraft. *Geophysical Research Letters*, *43*, 6713–6723. https://doi.org/10.1002/2016GL069260

Kanani, S., & Arridge, C. (2010). A new form of Saturn's magnetopause using a dynamic pressure balance model, based on in situ, multi-instrument Cassini measurements. *Journal of Geophysical Research*, *115*, A06207. https://doi.org/10.1029/2009JA014262

Kasahara, S., Kronberg, E. A., Krupp, N., Kimura, T., Tao, C., Badman, S. V., et al. (2011). Magnetic reconnection in the Jovian tail: X-line evolution and consequent plasma sheet structures. *Journal of Geophysical Research*, *116*, A11219. https://doi.org/10.1029/2011JA016892

Kellett, S., Bunce, E. J., Coates, A. J., & Cowley, S. W. H. (2009). Thickness of Saturn's ring current determined from north-south Cassini passes through the current layer. *Journal of Geophysical Research*, *114*, A04209. https://doi.org/10.1029/2008JA013942

Krimigis, S. M., Mitchell, D. G., Hamilton, D. C., Livi, S., Dandouras, J., Jaskulek, S., et al. (2004). Magnetosphere Imaging Instrument (MIMI) on the Cassini mission to Saturn/Titan. *Space Science Reviews*, *114*(1–4), 233–329. https://doi.org/10.1007/s11214-004-1410-8

Lai, H. R., Wei, H. Y., Russell, C. T., Arridge, C. S., & Dougherty, M. K. (2012). Reconnection at the magnetopause of Saturn: Perspective from FTE occurrence and magnetosphere size. *Journal of Geophysical Research*, *117*, A05222. https://doi.org/10.1029/2011JA017263

Liu, J., Angelopoulos, V., Zhang, X. J., Turner, D. L., Gabrielse, C., Runov, A., et al. (2016). Dipolarizing flux bundles in the cis-geosynchronous magnetosphere: Relationship between electric fields and energetic particle injections. *Journal of Geophysical Research: Space Physics*, *121*, 1362–1376. https://doi.org/10.1002/2015JA021691

Lewis, G. R., André, N., Arridge, C. S., Coates, A. J., Gilbert, L. K., Linder, D. R., & Rymer, A. M. (2008). Derivation of density and temperature from the Cassini-Huygens CAPS electron spectrometer. *Planetary and Space Science*, *56*(7), 901–912. https://doi.org/10.1016/j.pss.2007.12.017

Masters, A. (2015). The dayside reconnection voltage applied to Saturn's magnetosphere. *Geophysical Research Letters*, *42*, 2577–2585. https://doi.org/10.1002/2015GL063361

Masters, A., Eastwood, J. P., Swisdak, M., Thomsen, M. F., Russell, C. T., Sergis, N., et al. (2012). The importance of plasma β conditions for magnetic reconnection at Saturn's magnetopause. *Geophysical Research Letters*, *39*, L08103. https://doi.org/10.1029/2012GL051372

Masters, A., Mitchell, D. G., Coates, A. J., & Dougherty, M. K. (2011). Saturn's low-latitude boundary layer: 1. Properties and variability. *Journal of Geophysical Research*, *116*, A06210. https://doi.org/10.1029/2010JA016421

McAndrews, H. J., Owen, C. J., Thomsen, M. F., Lavraud, B., Coates, A. J., Dougherty, M. K., & Young, D. T. (2008). Evidence for reconnection at Saturn's magnetopause. *Journal of Geophysical Research*, *113*, A04210. https://doi.org/10.1029/2007JA012581

Mcandrews, H. J., Thomsen, M. F., Arridge, C. S., Jackman, C. M., Wilson, R. J., Henderson, M. G., et al. (2009). Plasma in Saturn's nightside magnetosphere and the implications for global circulation. *Planetary and Space Science*, *57*(14–15), 1–9. https://doi.org/10.1016/j.pss.2009.03.003

Mitchell, D. G., Brandt, P. C., Roelof, E. C., Dandouras, J., Krimigis, S. M., Mauk, B. H., et al. (2005). Energetic ion acceleration in Saturn's magnetotail: Substorms at Saturn? *Geophysical Research Letters*, *32*, L20S01. https://doi.org/10.1029/2005GL022647

Nakamura, R., Baumjohann, W., Klecker, B., Bogdanova, Y., Balogh, A., Rème, H., et al. (2002). Motion of the dipolarization front during a flow burst event observed by Cluster. *Geophysical Research Letters*, *29*(20), 1942. https://doi.org/10.1029/2002GL015763

Nakamura, R., Baumjohann, W., Mouikis, C., Kistler, L. M., Runov, A., Volwerk, M., et al. (2004). Spatial scale of high-speed flows in the plasma sheet observed by Cluster. *Geophysical Research Letters*, *31*, L09804. https://doi.org/10.1029/2004GL019558

Ohtani, S. I., Shay, M. A., & Mukai, T. (2004). Temporal structure of the fast convective flow in the plasma sheet: Comparison between observations and two-fluid simulations. *Journal of Geophysical Research*, *109*, A03210. https://doi.org/10.1029/2003JA010002

Øieroset, M., Lin, R. P., Phan, T. D., Larson, D. E., & Bale, S. D. (2002). Evidence for electron acceleration up to 300 keV in the magnetic reconnection diffusion region of Earth's magnetotail. *Physical Review Letters*, *89*(19), 195001. https://doi.org/10.1103/PhysRevLett.89.195001

Pan, Q., Ashour-Abdalla, M., Walker, R. J., & El-Alaoui, M. (2014). Electron energization and transport in the magnetotail during substorms. *Journal of Geophysical Research: Space Physics*, *119*, 1060–1079. https://doi.org/10.1002/2013JA019508

Pilkington, N. M., Achilleos, N., Arridge, C. S., Guio, P., Masters, A., Ray, L. C., et al. (2015). Internally driven large-scale changes in the size of Saturn's magnetosphere. *Journal of Geophysical Research: Space Physics*, *120*, 7289–7306. https://doi.org/10.1002/2015JA021290

Runov, A., Angelopoulos, V., Artemyev, A., Birn, J., Pritchett, P. L., & Zhou, X. Z. (2017). Characteristics of ion distribution functions in dipolarizing flux bundles: Event studies. *Journal of Geophysical Research: Space Physics*, *122*, 5965–5978. https://doi.org/10.1002/2017JA024010

Runov, A., Angelopoulos, V., Gabrielse, C., Liu, J., Turner, D. L., & Zhou, X. Z. (2015). Average thermodynamic and spectral properties of plasma in and around dipolarizing flux bundles. *Journal of Geophysical Research: Space Physics*, *120*, 4369–4383. https://doi.org/10.1002/2015JA021166

Runov, A., Angelopoulos, V., Gabrielse, C., Zhou, X. Z., Turner, D., & Plaschke, F. (2013). Electron fluxes and pitch-angle distributions at dipolarization fronts: THEMIS multipoint observations. *Journal of Geophysical Research: Space Physics*, *118*, 744–755. https://doi.org/10.1002/jgra.50121

Runov, A., Angelopoulos, V., Sitnov, M. I., Sergeev, V. A., Bonnell, J., McFadden, J. P., et al. (2009). THEMIS observations of an earthward-propagating dipolarization front. *Geophysical Research Letters*, *36*, L14106. https://doi.org/10.1029/2009GL038980

Runov, A., Angelopoulos, V., & Zhou, X. Z. (2012). Multipoint observations of dipolarization front formation by magnetotail reconnection. *Journal of Geophysical Research*, *117*, A05230. https://doi.org/10.1029/2011JA017361

Runov, A., Angelopoulos, V., Zhou, X. Z., Zhang, X. J., Li, S., Plaschke, F., & Bonnell, J. (2011). A THEMIS multicase study of dipolarization fronts in the magnetotail plasma sheet. *Journal of Geophysical Research*, *116*, A05216. https://doi.org/10.1029/2010JA016316

Russell, C. T., Jackman, C. M., Wei, H. Y., Bertucci, C., & Dougherty, M. K. (2008). Titan's influence on Saturnian substorm occurrence. *Geophysical Research Letters*, *35*, L12105. https://doi.org/10.1029/2008GL034080

Sergis, N., Arridge, C. S., Krimigis, S. M., Mitchell, D. G., Rymer, A. M., Hamilton, D. C., et al. (2011). Dynamics and seasonal variations in Saturn's magnetospheric plasma sheet, as measured by Cassini. *Journal of Geophysical Research*, *116*, A04203. https://doi.org/10.1029/2010JA016180

Sitnov, M. I., Swisdak, M., & Divin, A. V. (2009). Dipolarization fronts as a signature of transient reconnection in the magnetotail. *Journal of Geophysical Research*, *114*, A04202. https://doi.org/10.1029/2008JA03980

Slavin, J. A., Smith, M. F., Mazur, E. L., Baker, D. N., Hones, E. W., Iyemori, T., & Greenstadt, E. W. (1993). ISEE 3 observations of traveling compression regions in the Earth's magnetotail. *Journal of Geophysical Research*, *98*(A9), 15,425–15,446. https://doi.org/10.1029/93JA01467

Smith, A. W., Jackman, C. M., & Thomsen, M. F. (2016). Magnetic reconnection in Saturn's magnetotail: A comprehensive magnetic field survey. *Journal of Geophysical Research: Space Physics*, *121*, 2984–3005. https://doi.org/10.1002/2015JA022005

Sun, W. J., Fu, S. Y., Slavin, J. A., Raines, J. M., Zong, Q. G., Poh, G. K., & Zurbuchen, T. H. (2016). Spatial distribution of Mercury's flux ropes and reconnection fronts: MESSENGER observations. *Journal of Geophysical Research: Space Physics*, *121*, 7590–7607. https://doi.org/10.1002/2016JA022787

Sundberg, T., Slavin, J. A., Boardsen, S. A., Anderson, B. J., Korth, H., Ho, G. C., et al. (2012). Messenger observations of dipolarization events in Mercury's magnetotail. *Journal of Geophysical Research*, *117*, A00M03. https://doi.org/10.1029/2012JA017756

Thomsen, M. F. (2013). Saturn's magnetospheric dynamics. *Geophysical Research Letters*, *40*, 5337–5344. https://doi.org/10.1002/2013GL057967

Thomsen, M. F., Coates, A. J., Roussos, E., Wilson, R. J., Hansen, K. C., & Lewis, G. R. (2016). Suprathermal electron penetration into the inner magnetosphere of Saturn. *Journal of Geophysical Research: Space Physics*, *121*, 5436–5448. https://doi.org/10.1002/2016JA022692

Thomsen, M. F., Jackman, C. M., Mitchell, D. G., Hospodarsky, G., Kurth, W. S., & Hansen, K. C. (2015). Sustained lobe reconnection in Saturn's magnetotail. *Journal of Geophysical Research: Space Physics*, *120*, 10,257–10,274. https://doi.org/10.1002/2015JA021768

Thomsen, M. F., Mitchell, D. G., Jia, X., Jackman, C. M., Hospodarsky, G., & Coates, A. J. (2015). Plasmapause formation at Saturn. *Journal of Geophysical Research: Space Physics*, *120*, 2571–2583. https://doi.org/10.1002/2015JA021008

Thomsen, M. F., Reisenfeld, D. B., Wilson, R. J., Andriopoulou, M., Crary, F. J., Hospodarsky, G. B., et al. (2014). Ion composition in interchange injection events in Saturn's magnetosphere. *Journal of Geophysical Research: Space Physics*, *119*, 9761–9772. https://doi.org/10.1002/2014JA020489

Thomsen, M. F., Wilson, R. J., Tokar, R. L., Reisenfeld, D. B., & Jackman, C. M. (2013). Cassini/CAPS observations of duskside tail dynamics at Saturn. *Journal of Geophysical Research: Space Physics*, *118*, 5767–5781. https://doi.org/10.1002/jgra.50552

Tindale, E., & Chapman, S. C. (2016). Solar cycle variation of the statistical distribution of the solar wind ϵ parameter and its constituent variables. *Geophysical Research Letters*, *43*, 5563–5570. https://doi.org/10.1002/2016GL068920

Vasyliunas, V. M. (1983). *Plasma distribution and flow, Physics of the Jovian magnetosphere* (pp. 395–453). New York: Cambridge University Press. https://doi.org/10.1029/2003JD004173.Aires

Vogt, M. F., Kivelson, M. G., Khurana, K. K., Joy, S. P., & Walker, R. J. (2010). Reconnection and flows in the Jovian magnetotail as inferred from magnetometer observations. *Journal of Geophysical Research*, *115*, A06219. https://doi.org/10.1029/2009JA015098

Waite, J., & Furman, J. (2013). CASSINI orbiter SAT/SW CAPS derived electron moments V1.0, CO-S/SW-CAPS-5-DDR-ELE-MOMENTS-V1.0, NASA Planetary Data System.

Walsh, A. P., Owen, C. J., Fazakerley, A. N., Forsyth, C., & Dandouras, I. (2011). Average magnetotail electron and proton pitch angle distributions from Cluster PEACE and CIS observations. *Geophysical Research Letters*, *38*, L06103. https://doi.org/10.1029/2011GL046770

Yao, Z. H., Coates, A. J., Ray, L. C., Rae, I. J., Grodent, D., Jones, G. H., et al. (2017). Corotating magnetic reconnection site in Saturn's magnetosphere. *The Astrophysical Journal*, *846*(2), L25. https://doi.org/10.3847/2041-8213/aa88af

Yao, Z. H., Grodent, D., Ray, L. C., Rae, I. J., Coates, A. J., Pu, Z. Y., et al. (2017). Two fundamentally different drivers of dipolarizations at Saturn. *Journal of Geophysical Research: Space Physics*, *122*, 4348–4356. https://doi.org/10.1002/2017JA024060

Young, D. T., Berthelier, J. J., Blanc, M., Burch, J. L., Coates, A. J., Goldstein, R., et al. (2004). Cassini Plasma Spectrometer investigation. *Space Science Reviews*, *114*(1–4), 1–112. https://doi.org/10.1007/s11214-004-1406-4